

**DESIGN AND CONSTRUCTION OF AN ELECTRIC FIELD FOR HIGH  
PRECISION POLARIZABILITY MEASUREMENTS**

by

Gregory E. Schwarz

---

A Thesis Submitted to the Faculty of the

PHYSICS DEPARTMENT

In Partial Fulfillment of the Requirements  
For the Degree of

MASTER OF SCIENCE

In the Graduate College

THE UNIVERSITY OF ARIZONA

2 0 0 5

## STATEMENT BY AUTHOR

This thesis has been submitted in partial fulfillment of requirements for an advanced degree at The University of Arizona and is deposited in the Physics Department to be made available to students and faculty.

Brief quotations from this thesis are allowable without special permission, provided that accurate acknowledgment of source is made. Requests for permission for extended quotation from or reproduction of this manuscript in whole or in part may be granted by the head of the major department or the Dean of the Graduate College when in his or her judgment the proposed use of the material is in the interests of scholarship. In all other instances, however, permission must be obtained from the author.

SIGNED: \_\_\_\_\_

## APPROVAL BY THESIS DIRECTOR

This thesis has been approved on the date shown below

---

Alex Cronin  
Professor of Physics

---

Date

## ACKNOWLEDGMENTS

I wish to acknowledge the professors, teachers, colleagues, family and friends who have challenged me and encouraged me throughout my academic career. There are many who have had a considerable impact upon my development. In particular, I would like to thank Dr. Alex Cronin, my Masters Thesis chair. He guided my research and mentored me in my development as a physicist. He proofread numerous drafts of my thesis and provided invaluable feedback.

I also need to mention the help and support that John Perreault and Ben McMorran gave to me throughout the research and writing process. I am grateful to both of them for listening to the numerous techniques I considered using to solve engineering challenges. Their insights and feedback were very helpful. Additionally, I am grateful to Ben for the many times he listened as I practiced for my thesis defense.

I am also indebted to the U.S. Army for the opportunity to pursue a Masters Degree. I am grateful for its financial support.

I would also like to thank my wife Sarah and my daughter Virginia for their constant love and support. I am thankful to have such a devoted family.

# TABLE OF CONTENTS

<b>LIST OF FIGURES</b> . . . . .	6
<b>LIST OF TABLES</b> . . . . .	7
<b>ABSTRACT</b> . . . . .	8
<b>1 INTRODUCTION</b> . . . . .	9
1.1 Motivation . . . . .	10
1.2 Research Objectives . . . . .	11
1.2.1 Electric Field Model . . . . .	11
1.2.2 Electric Field Apparatus (EFA) . . . . .	11
1.2.3 Ratio Measurements of Polarizability . . . . .	12
<b>2 POLARIZABILITY THEORY</b> . . . . .	13
2.1 Neutral Atom in a Uniform Electric Field . . . . .	13
2.2 Metal Sphere in a Uniform Electric Field . . . . .	14
2.3 Mass on a Spring Model . . . . .	15
2.4 Stark Potential . . . . .	16
2.5 Summation of Oscillator Strengths . . . . .	16
<b>3 PREVIOUS ATOM INTERFEROMETER MEASUREMENTS OF POLARIZABILITY</b> . . . . .	18
3.1 Description of 1995 Polarizability Experiment . . . . .	18
3.2 Velocity Multiplexing . . . . .	21
3.3 Methods Employed to Improve the Geometry . . . . .	21
<b>4 ELECTRIC FIELD MODEL</b> . . . . .	24
4.1 The Method of Relaxation: Ground Zero . . . . .	24
4.2 Calculating $\int \mathbf{E}^2 dz$ . . . . .	29
4.3 Comparison to Semi-Infinite Capacitor . . . . .	34
4.4 The Algorithm of the FORTRAN Code . . . . .	37
4.5 Concluding Remarks on the Electric Field Model . . . . .	39
<b>5 ELECTRIC FIELD APPARATUS</b> . . . . .	41
5.1 Overview . . . . .	41
5.2 Components of the Apparatus . . . . .	42
5.2.1 Septum Electrode (SE) . . . . .	42
5.2.2 High Voltage Electrode (HVE) . . . . .	44

5.2.3	Substrate . . . . .	44
5.2.4	Frame, Spacers and Guard Electrodes . . . . .	46
5.3	Assembling the EFA . . . . .	47
5.4	Critical Geometric Measurements . . . . .	49
5.4.1	Separation of the Electrodes . . . . .	49
5.4.1.1	Laser Interferometer Techniques . . . . .	49
5.4.1.2	Fabry-Perot Optical Interference Fringe Pattern . . . . .	50
5.4.2	Length of the High Voltage Electrode . . . . .	50
5.4.2.1	Contributions to the Uncertainty in $L$ . . . . .	51
5.5	Evaluation of a Prototype . . . . .	51
5.5.1	Breakdown Voltage . . . . .	52
5.5.2	Determining $L_{eff}/L$ . . . . .	52
5.5.3	Calculated Phase Shift . . . . .	53
<b>6</b>	<b>PERFORMING A RATIO MEASUREMENT . . . . .</b>	<b>61</b>
<b>7</b>	<b>SUMMARY . . . . .</b>	<b>64</b>
<b>8</b>	<b>FUTURE WORK . . . . .</b>	<b>65</b>
8.1	EFA . . . . .	65
8.2	Electric Field Modeling Program . . . . .	65
	<b>Appendix A. Sample FORTAN 5-point Scheme Rectangular Grid Code</b>	<b>67</b>
	<b>Appendix B. FORTRAN 9-point Averaging Scheme . . . . .</b>	<b>76</b>
	<b>REFERENCES . . . . .</b>	<b>77</b>

## LIST OF FIGURES

3.1	Schematic of the Mach-Zender Atom Interferometer . . . . .	18
3.2	Geometry of 1995 Interaction Region . . . . .	19
4.1	Grid notation for averaging equations. . . . .	24
4.2	Difference plot region . . . . .	27
4.3	Difference plot of 5-point and 9-point scheme for no guard electrodes . . . . .	28
4.4	Difference plot of 5-point and 9-point scheme for 1995 guard electrode geometry . . . . .	29
4.5	Difference plot of 5-point and 9-point scheme for wrap-around guard electrode geometry . . . . .	29
4.6	Potential plot of 1995 Geometry with original guard electrodes . . . . .	30
4.7	Potential plot of 1995 Geometry with wrap-around guard electrodes . . . . .	31
4.8	1995 Geometry with original guard electrodes. . . . .	32
4.9	1995 Geometry with wrap-around guard electrodes. . . . .	33
4.10	Effect of boundary on the numerical solution as compared to the analytical solution for a semi-infinite capacitor . . . . .	35
4.11	Comparison of semi-infinite capacitor potential lines to the numerical solution near the end of the electrode . . . . .	36
4.12	Diagram of Relaxation Region . . . . .	37
5.1	Geometry of desired 2005 EFA . . . . .	43
5.2	Position of the EFA inside the atom beam . . . . .	43
5.3	$\Delta L/L$ vs Temperature for various possible substrate materials . . . . .	46
5.4	Illustration of the Substrate showing the scale of the main groove . . . . .	47
5.5	Photograph of 2in by 2in square pyrex with silicon bonded to the surface . . . . .	47
5.6	Anodic Bonding Diagram . . . . .	48
5.7	2005 Electric Field Apparatus prototype pictures. . . . .	55
5.8	Picture of the Prototype Groove . . . . .	56
5.9	Picture of the Prototype Septum Surface and Guard Electrodes . . . . .	56
5.10	Fringe data for two plates separating from contact. . . . .	57
5.11	Photo of fringe pattern using 632.8 nm laser light . . . . .	58
5.12	Support Structure Considerations . . . . .	59
5.13	1995 and 2005 Electric Field Apparatus $L/L_{eff}$ Plots . . . . .	60
6.1	Benefits of Wrap-Around Electrodes to a Ratio Measurement . . . . .	62
8.1	Future Relaxation Grid Boundary Recommendation . . . . .	66

## LIST OF TABLES

3.1	Relative contributions of geometric error sources the to 1995 polarizability measurements. . . . .	21
4.1	Line integrals, $\int_0^{10cm} \mathbf{E}^2 dz$ , for original guard electrodes. . . . .	31
4.2	Line integrals, $\int_0^{10cm} \mathbf{E}^2 dz$ , for wrap-around guard electrode geometry. . .	31
5.1	Relative contributions of geometric error sources to the measured polarizability for the 2005 EFA. . . . .	54

## ABSTRACT

Research has been conducted to design and construct an electric field for high precision polarizability measurements.

The primary area of research was to investigate materials and techniques needed to create a precision electric field. The precision electric field required one electrode to be very thin,  $\sim 10\text{-}30\mu\text{m}$ . I developed a method to observe changes in the separation between the electrodes using a Fabry-Perot interferometer. Additionally, the new geometry reduced the phase gradient near the septum electrode. By increasing the geometric precision of the electric field and using a dispersion compensation technique, the uncertainty in the polarizability of sodium could be reduced by nearly a factor of two.

The secondary area of research involved writing a program to model the electric fields. The program provided a method to compare interaction region geometries.

# CHAPTER 1

## INTRODUCTION

The polarizability of an atom or molecule describes its response to an external electric field. In general, the polarizability of a system is a tensor quantity, because non-spherically symmetric systems get polarized by different amounts and in different directions depending on their orientation in the external electric field. For isolated alkali atoms and DC electric fields, the polarizability is essentially a scalar. The atomic polarizability that I am interested in measuring is the static, ground state, electric dipole polarizability.

The electric dipole polarizability,  $\alpha$ , describes an atom's response in the lowest order to an external electric field. For a neutral atom, such as the alkali metals, the electric dipole polarizability can be defined by the equation

$$\vec{p} = \alpha \vec{E} \tag{1.1}$$

where  $\vec{p}$  is the electric dipole moment and  $\vec{E}$  is the applied external electric field.

The polarizability of atoms has been studied for nearly a century. Miller and Bederson [1] provide a detailed description of theoretical and experimental methods used up to 1977. Most atom beam techniques used to measure the polarizability of alkali metals used deflection in electric field gradients. In 1993, Ekstrom et al. [2], used an atom interferometer to make the most precise measurement of sodium polarizability to date. The specific atom interferometer used in the experiment is described in detail by J. Schmiedmayer et al. [3]. The interferometer is a Mach-Zender type in an apparatus that is close to four meters long. The atoms in the 1995 experiment were diffracted using 200nm period nanostructure gratings. This interferometer puts the atoms in a

superposition of center of mass states that propagate in two spatially separated paths referred to as the arms of the interferometer. The two arms of the interferometer are separated so that one arm of the interferometer passes through a uniform electric field, and the other does not. The electric field imparts a phase shift to the atomic de Broglie waves which results in a spatial translation (i.e. phase shift) of the interference fringes at the output of the interferometer. The phase shift as a function of applied electric field allows the determination of the polarizability of the atomic species.

## 1.1 Motivation

There are several motivations for this project. The main motivation is to extend the use of atom interferometry to measure the polarizability of all of the alkali metals more accurately. For this a precisely built and characterized interaction region is needed. A list of nine papers [4, 5, 6, 7, 8, 9, 10, 11, 12] as well as a 2005 paper by A. J. Thakkar [13] all report theoretical results for the polarizability of Na. This is evidence that the scientific community is currently interested in increasing the accuracy of polarizability measurements. The debate over whether sodium or lithium has a larger polarizability has been ongoing for nearly 30 years, and the techniques explained in this thesis could provide the hardware necessary to experimentally answer this question.

Because polarizability is a fundamental characteristic of each element and molecule, increasing the precision by which it is known extends to many areas of atomic physics. The long-range electron-atom or ion-atom interaction energy, the van der Waals interaction between neutral atoms and the index of refraction of gases are all areas in which the polarizability of the atoms contribute to the physical behavior of the system. Atomic state lifetimes and atomic transition oscillator strengths also depend on similar physics as the polarizability (i.e. the dipole matrix elements).

## 1.2 Research Objectives

The primary research objective is to create a more precisely known electric field to facilitate the measurement of atomic polarizability of atoms with an accuracy of 0.1%. In order to build a more precisely known electric field, we must accurately characterize the geometry of the interaction region and the field produced by it.

The second goal is to establish a methodology to determine the ratio of the polarizability of sodium to the polarizability of lithium with a precision of 0.01%. My main contributions to this research are the development of new techniques to make an electric field apparatus and the development of a numerical model of the electric field produced by it. Next, I will discuss the main areas of research necessary to achieve these objectives.

### 1.2.1 Electric Field Model

To measure polarizability, the line integral  $\int |\vec{E}|^2 dz$  along both arms of the interferometer must be known to better than 0.1%. I have modeled  $\vec{E}$  at all points along these paths using the method of relaxation, and worked on ways to put a bound on the error in the line integral due to the calculation of  $\vec{E}(x, z)$  on a 2D lattice. I have also used the  $\vec{E}$  model to show how the guard electrode configurations effect the phase gradient acquired by the atom beam on both sides of the septum electrode.

### 1.2.2 Electric Field Apparatus (EFA)

The desired specifications of the electric field apparatus (EFA) are to:

- mount a 10-30 $\mu$ m thick septum electrode that is flat to within 10 $\mu$ m over a length of 5cm and permits passage of an atom beam on either side,
- construct a parallel plate capacitor using the septum electrode and a high voltage electrode,

- quantify how the septum electrode moves when voltage is applied,
- create a minimum of a 200 radian phase difference between the two interferometer arms (by increasing the phase difference slowly the total amount is determined),
- decrease the phase gradient across the atom beam by suppressing the fringing fields, and
- know the geometry accurately enough to calculate the line integral,  $\int |\vec{E}|^2 dz$ , to a precision of 0.1%.

### 1.2.3 Ratio Measurements of Polarizability

Performing a ratio measurement would remove much of the uncertainty due to the geometry of the electric field apparatus. The geometric uncertainties of the EFA would be common to both measurements and therefore not effect the ratio. By eliminating the geometric uncertainty and using the rephasing technique [14], the ratio of the two polarizabilities would be accurate to approximately 0.01%. The ratio measurement is possible because each atom species' polarizability can be measured using the same portion of the interaction region. Still, measuring or compensating for the velocity of the atoms in the beam would be needed for ratio measurements.

## CHAPTER 2

### POLARIZABILITY THEORY

Electric polarizability is commonly reported using cgs units of  $\text{cm}^3$ . A general equation to transition between units is

$$\alpha_{cgs} = \frac{\alpha_{SI}}{4\pi\epsilon_0}. \quad (2.1)$$

When SI units for polarizability are used, it is common for a table to list  $\frac{\alpha}{4\pi\epsilon_0}$  and use units of  $\text{m}^3$  or  $\text{\AA}^3$  so as to report the polarizability in familiar units of length cubed. Later in this thesis, equations are in cgs units unless stated otherwise.

#### 2.1 Neutral Atom in a Uniform Electric Field

A simple model for calculating the polarizability of a neutral atom assumes the positively charged nucleus is surrounded by a spherical electron cloud with uniform negative charge density [15]. I use cgs units in this example. If the nucleus is displaced a distance  $d$  from the center of the electron cloud it creates a dipole moment,

$$\vec{p} \equiv q\vec{d} \quad (2.2)$$

where  $q$  is the charge of the nucleus. The electric field produced by the electron cloud on the nucleus is

$$-\vec{E} = \frac{q\vec{d}}{a^3} \quad (2.3)$$

where  $a$  is the electron cloud radius. If an external electric field induces this dipole, then in equilibrium the external electric field is equal in magnitude and opposite in direction to the field made by the electron cloud. Substituting Eqs. (2.2) and (2.3) into Eq. (1.1)

and solving for  $\alpha$ , one finds that

$$\alpha = a^3 \quad (2.4)$$

Which means that in this model the polarizability of a neutral atom is the cube of the atomic radius. An approximation of the atomic radius of Na is  $2.1649\text{\AA}$  [16], which makes the polarizability  $10.146 \times 10^{-24} \text{cm}^3$ . The measured value for Na is  $24.11(12) \times 10^{-24} \text{cm}^3$ .

## 2.2 Metal Sphere in a Uniform Electric Field

In this example, the neutral atom is modeled as an uncharged, conducting sphere with radius  $a$ , isolated in a uniform electric field. Griffiths [15] and Jackson [17] show how to solve for the potential outside the sphere and the corresponding surface charge density on the surface of the sphere. While the techniques used to solve for the potential and surface charge distribution are more involved than the first example, the final result is the same. The equations in this section are written in SI units. Fitting the boundary conditions at the surface of the sphere and far from the surface of the sphere with a function of the form

$$V(r, \theta) = \sum_{l=0}^{\infty} \left( A_l r^l + \frac{B_l}{r^{l+1}} \right) P_l(\cos \theta) \quad (2.5)$$

the potential outside the sphere is

$$V(r, \theta) = -E_0 \left( r - \frac{a^3}{r^2} \right) \cos \theta \quad (2.6)$$

The surface charge density on the sphere is

$$\sigma(\theta) = -\epsilon_0 \left. \frac{\partial V}{\partial r} \right|_{r=a} = 3\epsilon_0 E_0 \cos \theta. \quad (2.7)$$

As evident by the  $\cos \theta$  term, there is no charge at  $\theta = \frac{\pi}{2}$ , and two hemispheres have opposite charge. The charge distribution on the surface is equivalent to a dipole moment with the magnitude

$$p = 4\pi\epsilon_0 E_0 a^3. \quad (2.8)$$

Substituting Eq. (1.1) into Eq. (2.8) and solving for the polarizability you get

$$\alpha = 4\pi\epsilon_0 a^3 \quad (2.9)$$

which is the same result as the electron cloud picture.

### 2.3 Mass on a Spring Model

A simple model for a neutral atom in a uniform electric field is to represent the opposite charges of the dipole as charged masses connected by a spring. This picture is also explained by Ekstrom in this Ph.D. thesis [18]. This section uses cgs units. The massive nucleus is essentially stationary and the electron is acted on by the external electric field until the forces balance and the equilibrium equation is

$$eE = kd \quad (2.10)$$

where  $e$  is the charge of the electron,  $E$  is the magnitude of the external electric field,  $k$  is the spring constant, and  $d$  displacement of the electron. Using the equation  $\omega = \sqrt{\frac{k}{m}}$ , one can write the equation for the dipole moment in terms of the resonant frequency,  $\omega_0$ :

$$p = ed = \frac{e^2 E}{m_e \omega_0^2}. \quad (2.11)$$

Using Eq. (1.1), one can solve for the static polarizability to get

$$\alpha = \frac{e^2}{m_e \omega_0^2}. \quad (2.12)$$

For sodium, there is one electron transition that dominates (i.e. has the largest oscillator strength) and that is the Na D line (3s to 3p transition) which has a frequency,  $\omega_0 = 3.200 \times 10^{15}$  Hz. Using cgs values of  $e = 4.802 \times 10^{-10}$  esu ( $\text{esu} = \sqrt{\frac{g \text{ cm}^3}{s^2}}$ ) and  $m_e = 9.109 \times 10^{-28}$  g, the polarizability for sodium is calculated to be  $24.7 \times 10^{-24}$  cm<sup>3</sup>. This theoretical calculation for the polarizability gives a value that corresponds much better with experiment than the previous method.

## 2.4 Stark Potential

For moderate field strengths the equation,  $\vec{p} = \alpha\vec{E}$ , correctly describes the induced dipole moment of spherically symmetric, neutral atoms with no permanent electric-dipole moment. The Stark potential is equal to the energy necessary to create an electric dipole moment. I will write everything in terms of magnitudes since the vectors are all in one dimension. The work done by the external electric field to create a dipole moment is

$$W = \int F_e dx. \quad (2.13)$$

Substituting in  $F = qE$  and using the differential form of Eq. (2.2) and (1.1) to perform a change of variables, the integral can be written as

$$W = \alpha \int E dE \quad (2.14)$$

and integrated to arrive at

$$W = \frac{1}{2}\alpha E^2. \quad (2.15)$$

This is the work done by the electric field on the atom to create a dipole. It is also equal to the ground state energy shift for the atom. The ground state energy gets shifted by

$$U_{Stark} = -W = -\frac{1}{2}\alpha|\vec{E}|^2. \quad (2.16)$$

The negative sign here means that work is required to move the polarized atom out of the region of non-zero electric field.

## 2.5 Summation of Oscillator Strengths

Miller and Bederson [1] described this method of calculating the polarizability in detail. It is common to represent the external electric field as a small perturbation described by the potential energy of the interaction,  $U = -\vec{p} \cdot \vec{E}$ , where  $\vec{p} = -e \sum_{i=0}^N \langle \vec{r}_i \rangle$

and  $N$  is the number of electrons in the atom. The first-order energy correction is

$$E^{(1)} = \langle \Psi_0 | \vec{p} \cdot \vec{E} | \Psi_0 \rangle, \quad (2.17)$$

and it equals zero for any state with definite parity. The second order energy correction is written as

$$E^{(2)} = -|\vec{E}|^2 \sum_{k \neq 0} \frac{|\langle \Psi_0 | \vec{p} \cdot \hat{n} | \Psi_k \rangle|^2}{\mathcal{E}_k - \mathcal{E}_0} \quad (2.18)$$

where  $\hat{n}$  is a unit vector in the direction of  $\vec{E}$ . Comparing this equation to Eq. 2.16, the polarizability can be written as

$$\alpha = \frac{e^2 \hbar^2}{m_e} \sum_{k \neq 0} \frac{f_{0,k}}{(\mathcal{E}_k - \mathcal{E}_0)^2} \quad (2.19)$$

where  $f_{0,k}$ , the oscillator strength, is defined as

$$f_{0,k} \equiv \frac{2m_e}{e^2 \hbar^2} |\langle \Psi_0 | \vec{p} \cdot \vec{n} | \Psi_k \rangle|^2 (\mathcal{E}_k - \mathcal{E}_0) \quad (2.20)$$

for a given transition. Because the oscillator strength of the primary transition from the ground state is almost exactly one for sodium and all other oscillator strengths combined are much less than one, the oscillator sum method does not change the polarizability calculation for sodium significantly. In 1959, Dalgarno and Kingston [19] used the oscillator strength sum rule to calculate the polarizability of sodium to be  $24.6 \times 10^{-24} \text{ cm}^3$ . Note that the dipole matrix elements in Eq. 2.18 also contribute to state lifetimes, decay rates, van der Waals coefficients and oscillator strengths. Thus, measurements of polarizability can test the theory used to predict all of these quantities.

# CHAPTER 3

## PREVIOUS ATOM INTERFEROMETER MEASUREMENTS OF POLARIZABILITY

### 3.1 Description of 1995 Polarizability Experiment

In 1995, C.R. Ekstrom et al. [2] experimentally determined the polarizability of sodium to be  $24.11(6)_{\text{statistical}}(6)_{\text{systematic}} \times 10^{-24} \text{cm}^3$ . Adding the systematic and statistical uncertainties in quadrature gives an uncertainty of 0.35% in the polarizability.

The experimental apparatus he used is a three-grating Mach-Zender interferometer with a metal foil physically isolating the two beams, see Fig. 3.1. The specifics about the atom interferometer are detailed by Ekstrom in his Ph.D. thesis [18]. In his analysis of the electric field, he found that the use of guard electrodes greatly reduced the phase-gradient across the width of the beam. The final measurement of sodium's polarizability was made using an interaction region with guard electrodes.

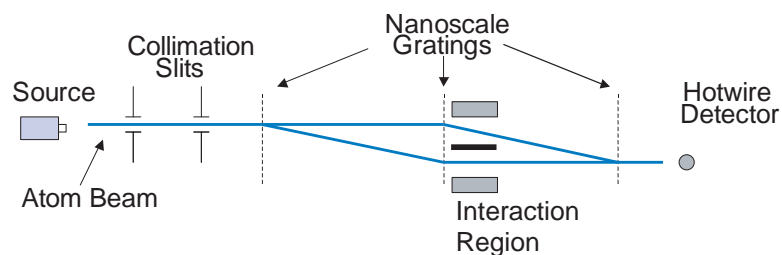


Figure 3.1: Schematic of the Mach-Zender Atom Interferometer used for making the polarizability measurements.

The interaction region is constructed by stretching a metal foil symmetrically between two side electrodes. Insulating, alumina spacers with precise dimensions of 0.1% accuracy are between the foil and the side electrodes. The foil has a nominal thickness of  $10\mu\text{m}$ . The foil is stretched so as to pull out all the wrinkles before it is clamped between the spacers, side

electrodes, and a mounting clamp. A cross-section view of the interaction region with guard electrodes is shown in Fig. 3.2. The interaction region is mounted on a stage with three

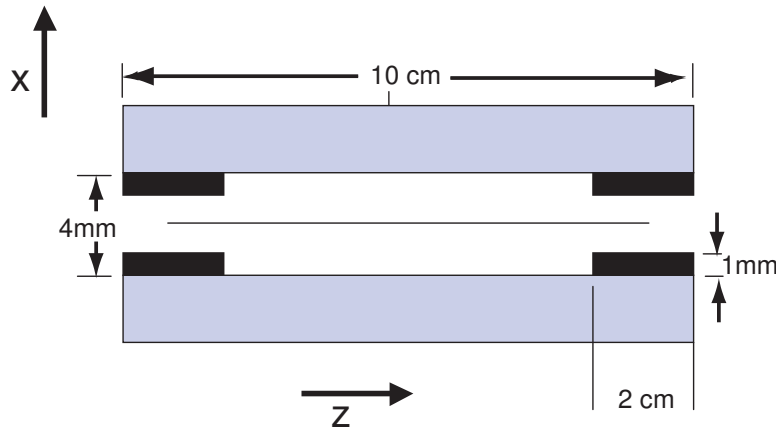


Figure 3.2: Figure taken from Ekstrom [18]. Details the geometry of the 1995 interaction region viewed from above. The side electrodes are shown in gray and either one or both can be elevated to high voltage. The horizontal line in the center is the metal foil. The guard electrodes are shown in black and are held at the same potential as the metal foil. Each guard electrode consists of an insulating support and a metal layer on one or both sides.

motors that allows the interaction region to move in and out of the beam line, to make the foil oriented with respect to the collimation slits axis of the beam and to make the foil oriented with respect to the direction of the beam. A typical 10cm long septum would cast a shadow of  $20\text{-}30\mu\text{m}$  even though the foil was only  $10\mu\text{m}$  thick. The increase in thickness is attributed to imperfections in the foil after it is stretched. Regardless, the conducting, physical barrier was thin enough to allow one arm of the interferometer to pass through an electric field and the other arm to pass outside the electric field.

As described by Ekstrom [2, 18], the experimental method involved measuring the phase shift of the atoms when they move through the potential  $U(x)$  created by the interaction region. The phase evolution of the wave function of the atom beam can be written with in the JWKB approximation as

$$\Psi(z) = \Psi(0)e^{i \int_0^z k(z) dz} \quad (3.1)$$

where  $k(z) = \frac{1}{\hbar} \sqrt{2m(E - U(z))}$ . The potential is applied to one arm of the interferometer and the resulting phase difference between the two arms is

$$\Delta\phi = \int k(z)dz - \int k_0 dz \simeq -\frac{1}{\hbar v} \int U(z)dz \quad (3.2)$$

In this experiment, because the electric field is nearly uniform, the energy of the arm passing through the interaction region is shifted by the Stark potential,

$$U(z) = -\frac{1}{2}\alpha|\vec{E}(z)|^2 \quad (3.3)$$

where  $\vec{E}(z)$  is the magnitude of the electric field at location  $z$ . From the measured phase shift,  $\Delta\phi$ , the polarizability can be reported using the relation

$$\alpha = \left(\frac{\Delta\phi}{V^2}\right) \left(\frac{D^2}{L_{eff}}\right) (2\hbar v) \quad (3.4)$$

where  $V$  is the voltage,  $D$  is the separation between the electrodes,  $L_{eff}$  is the effective length of the capacitor, and  $v$  is the velocity of the atom beam. Eq. (3.4) requires all cgs units. The effective length of the capacitor,  $L_{eff}$ , is defined as

$$\left(\frac{V}{D}\right)^2 L_{eff} \equiv \int |\vec{E}|^2 dx. \quad (3.5)$$

Ekstrom plotted  $L_{eff}/L$  for paths  $50\mu\text{m}$  on either side of the septum where  $L$  is the true length capacitor. This ratio is a method to illustrate whether atoms passing different distances from the beam get the same phase shift. His analysis showed that the guard electrodes made the ratio  $L_{eff}/L$  much more constant for distances 20 to  $50\mu\text{m}$  away from the septum. With the guard electrodes the ratio  $L_{eff}/L$  varied by less than one part in 1000 on both sides of the septum. Similar analysis will be repeated here for a variety of guard electrode configurations.

The sources of uncertainty were the geometry of the interaction region, the determination of the velocity distribution of the atom beam, and the short term stability of the phase reference in the experiments. The geometric uncertainty of the interaction region reduces down to errors from two sources: the separation distance  $D$  and the effective length of the interaction region,  $L_{eff}$ , Eq. (3.5). The separation distance  $D$  was assumed to be the thickness of the spacers with small adjustments due to spacers varying along their length.  $L_{eff}$  represents the length

Table 3.1: Relative contributions of geometric error sources the to 1995 polarizability measurements.

Error Source	Systematic Error in $\alpha$
Spacer width, $D$ ( $2.0\text{mm}\pm 1\mu\text{m}$ )	0.07%
Interaction region length, $L$ ( $6.0\text{cm}\pm 25\mu\text{m}$ )	0.08%
Electric field calculation correction ( $L_{eff}/L$ ) ( $0.98\pm 10^{-3}$ )	0.10%

of an ideal capacitor that would cause an equal phase shift,  $\Delta\phi$ , to that caused by the finite length capacitor, of length  $L$ , including its fringing fields. Although not explicitly stated, the uncertainty in the interaction region length,  $L$ , is due to the uncertainty in the measurement as well as the uncertainty due to the exact path of the atom beam. The uncertainty in  $L_{eff}$  comes from the uncertainty in the electric fields which were determined by standard methods of relaxation. The systematic errors in the polarizability due to the geometric uncertainties are listed in Table 3.1.

## 3.2 Velocity Multiplexing

Roberts et al. [14] describe how the use of a rephasing technique completely eliminates the problems associated with the spread of velocities in the atom beam and, for example, the systematic uncertainty due to the mean velocity and the velocity distribution of the atom beam. The authors state the use of this technique could enable a ratio measurement of electric polarizabilities with precision of one part in 10,000.

Since Roberts et al. developed a dispersion compensation technique to reduce these uncertainties, it is my intention to reduce the geometric uncertainties.

## 3.3 Methods Employed to Improve the Geometry

In his Ph.D. thesis, Roberts [20] wrote a section on how to overcome the geometry errors. An improved measurement of the absolute polarizability must improve the precision of the three

parameters,  $D$ ,  $L$  and  $L_{eff}$ , listed in Table 3.1. His list of improvements is very comprehensive, and I have incorporated several of the techniques he suggests in developing a new interaction region. I have also incorporated some new ideas to accomplish the same goals of reducing the geometric uncertainties.

Roberts suggests using an optical interferometer to measure the separation distance  $D$ . I have several ideas for methods to make an absolute measurement of  $D$  with optical interferometry, but I was not able to make them work accurately enough. I made a Fabry-Perot interferometer between the high voltage electrode and the septum electrode. Using the interferogram, the uncertainty in the separation distance can be reduced. While not done in this project, the knowledge of how the surface changes could be incorporated in the model of the electric field to decrease the uncertainty due to  $D$ .

Roberts suggests an improved numerical modeling of the electric field to improve the accuracy of  $L_{eff}/L$ . I do not know the exact method used in the 1995 experiment, but I attempted to use an averaging method in which I can put a bound on the error due to the averaging method itself. I also wish to include uncertainty due to variations in  $D$ ,  $L$ , the length of the guard electrodes, the length of the septum, and the separation between the guard electrodes and the septum.

Roberts suggests better construction so that the septum remains very flat and does not sag, as was the case for the foil if the tension in it was lost. I have used a technique known as anodic bonding to firmly attach metalized silicon slab to one of the side electrodes. This bond is very strong and prevents the silicon from sagging, even when the desired voltage is applied to the high voltage electrode. The silicon remained flat to within  $10\mu\text{m}$  by this method and is locally flat enough to permit optical interferometry, unlike the foil.

Roberts suggests to make the guard electrodes and septum longer to eliminate the need to characterize the fringing fields seen by the beam passing on the zero-field side of the capacitor. I agree that eliminating the field seen by the zero-field side beam is important. I have investigated wrapping the guard electrodes around the high voltage electrode so as to eliminate more of the

fringing fields. Even just partially closing it in, virtually eliminates the electric field outside the capacitor.

## CHAPTER 4

### ELECTRIC FIELD MODEL

The purpose of the electric field modeling program is to calculate  $\oint \mathbf{E}^2 dl$  for atom beam paths through the EFA. The paths generally run very close by the septum electrode, but due to the thickness of the atom beam, they may span  $20\mu\text{m}$  and due to misalignment of the EFA in the interferometer they may span  $50\mu\text{m}$ . From the value for  $\int \mathbf{E}^2 dl$ , the value for  $L_{eff}$  can be determined. The modeling program was also used to evaluate various geometries of guard electrodes in order to find the configurations that produced the most uniform electric field. The modeling program was also used to quantify how small geometric misalignments cause changes in the  $\int \mathbf{E}^2 dl$ . These changes were used to approximate the uncertainty in  $L_{eff}$ . A uniform electric field would have  $L_{eff}=L$  for all paths, but fringing fields and imperfect construction of the EFA cause  $L_{eff}$  to be different from the physical length  $L$  of the high voltage electrode (HVE). A separate goal of this section is to quantify the uncertainty in the numerical techniques so that we can be sure they are working well enough to use in our analysis.

#### 4.1 The Method of Relaxation: Ground Zero

To solve Laplace's equation,  $\nabla^2 V = 0$ , numerically, one can evaluate the potential  $V(\vec{r})$  at each point on a lattice in terms of the potential at neighboring points and then iterate this

$$\begin{array}{ccc}
 \bullet V_{i-h,j+h} & \bullet V_{i,j+h} & \bullet V_{i+h,j+h} \\
 \bullet V_{i-h,j} & \bullet V_{i,j} & \bullet V_{i+h,j} \\
 \bullet V_{i-h,j-h} & \bullet V_{i,j-h} & \bullet V_{i+h,j-h}
 \end{array}$$

Figure 4.1: Grid notation for averaging equations.

technique for the entire lattice several times. Due to the symmetry of the interaction region, we can model it on a 2-D lattice. In more detail, one expands several Taylor series and solves for the sum of the two spacial second derivatives. The simplest method is to use the series for the four points exactly one grid spacing away from the point you are calculating. Using the notation in Fig. 4.1, the following are the series written for the four points, or nodes, adjacent to the center point. For the two points in the x direction, the two series are

$$V(i+h, j) = V(i, j) + h \frac{dV}{dx} + \frac{h^2}{2} \frac{d^2V(i, j)}{dx^2} + \frac{h^3}{3!} \frac{d^3V(i, j)}{dx^3} + \frac{h^4}{4!} \frac{d^4V(i, j)}{dx^4} + \frac{h^5}{5!} \frac{d^5V(i, j)}{dx^5} + O(h^6) \quad (4.1)$$

and

$$V(i-h, j) = V(i, j) - h \frac{dV}{dx} + \frac{h^2}{2} \frac{d^2V(i, j)}{dx^2} - \frac{h^3}{3!} \frac{d^3V(i, j)}{dx^3} + \frac{h^4}{4!} \frac{d^4V(i, j)}{dx^4} - \frac{h^5}{5!} \frac{d^5V(i, j)}{dx^5} + O(h^6). \quad (4.2)$$

There are two very similar equations for the two points in the y direction. By summing the four equations and solving for  $V(i, j)$ , you will get

$$V(i, j) = \frac{1}{4}[V(i+h, j) + V(i-h, j) + V(i, j+h) + V(i, j-h)] + h^2 \nabla^2 V(i, j) - \frac{h^4}{48} \left( \frac{d^4V(i, j)}{dx^4} + \frac{d^4V(i, j)}{dy^4} \right) - O(h^6). \quad (4.3)$$

Substituting in  $\nabla^2 V(i, j) = 0$ . Truncating the series at  $O(h^4)$ , the discrete Laplace's equation is

$$V(i, j) = \frac{1}{4}[V(i+h, j) + V(i-h, j) + V(i, j+h) + V(i, j-h)] \quad (4.4)$$

and the leading error term is the  $O(h^4)$  from Eq. (4.3). In the literature, this technique is commonly referred to as the 5-point averaging method. One can perform a similar process with the four diagonal points,  $V(i+h, j+h)$ ,  $V(i+h, j-h)$ ,  $V(i-h, j+h)$ , and  $V(i-h, j-h)$  and improve the accuracy of the calculation for  $V(i, j)$ . Using the Taylor expansion in two

dimensions, summing the four series, and substituting in  $\nabla^2 V(i, j) = 0$ , one arrives at

$$\begin{aligned}
 V(i, j) = & \frac{1}{4}[V(i+h, j+h) + V(i+h, j-h) + \\
 & V(i-h, j+h) + V(i-h, j-h)] + \\
 & \frac{h^4}{3} \left( \frac{d^4 V(i, j)}{dx^4} + \frac{d^4 V(i, j)}{dy^4} \right) + O(h^6).
 \end{aligned} \tag{4.5}$$

By weighting (4.3) and (4.5) properly and summing them, one can exactly eliminate the  $O(h^4)$  term so that the leading error term is  $O(h^6)$ . This method is often referred to in the literature as the 9-point method, and the final averaging equation is

$$\begin{aligned}
 V(i, j) = & \frac{1}{5}[(V(i+h, j) + V(i-h, j) + V(i, j+h) + V(i, j-h)] + \\
 & \frac{1}{20}[V(i+h, j+h) + V(i+h, j-h) + V(i-h, j+h) + V(i-h, j-h)] + \\
 & O(h^6).
 \end{aligned} \tag{4.6}$$

In this manner, it is possible to determine where the largest error occurs, which is primarily due to the  $O(h^4)$  error term for the 5-point averaging method. Since the  $O(h^6)$  terms and higher are not equal for the two averaging schemes, the difference is not exactly the  $O(h^4)$  term for the 5-point averaging method.

An alternative would be to calculate the discrete fourth-derivative using the potential grid created by the 5-point averaging method. But in taking the discrete fourth order derivative, you would introduce some additional error from truncating the Taylor series used to write the discrete fourth order derivative.

When solving Laplace's equation by numerical methods, the potential is approximated by a discretely evaluated function with special continuity conditions imposed on the boundaries and the potential is determined throughout the region by minimizing the electrostatic energy by iteration [21]. By making the grid more dense, i.e. with smaller  $h$ , the values of the potential at each point become more accurate. By including more points in the averaging scheme to

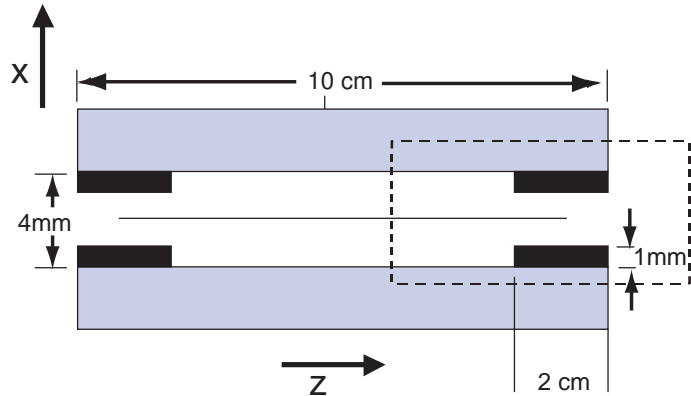


Figure 4.2:

The difference plots in Figs. 4.3, 4.4 and 4.5 are approximately the region outlined with the dashed line.

make the leading order error term of higher order  $h$ , the values of the potential at each point become more accurate.

For the 5-point averaging method, the sum of the error terms is

$$\sum_{n=2}^{\infty} \frac{2h^{2n}}{(4)(2n)!} \left( \frac{d^{2n}V(i, j)}{dx^{2n}} + \frac{d^{2n}V(i, j)}{dy^{2n}} \right). \quad (4.7)$$

The numerical solution to Laplace's equation will always converge, therefore, this series will converge. The question is, how fast does it converge? The answer to that question depends on where in the grid you are concerned with. By looking at the difference in the 5-point and 9-point averaging schemes for a region containing a parallel plate capacitor, I can qualitatively show that the largest error due to the averaging method is small regions near sharp points and corners where the higher order derivatives in Eq. 4.7 are largest. The regions with higher order derivatives are also the regions with the largest fringing fields. I have chosen to illustrate this using three plots of the difference between the 5-point and 9-point schemes using the same geometry except for the type of guard electrodes. The three plots illustrate the part of the interaction region as shown in Fig. 4.2. Figures 4.3, 4.4 and 4.5 illustrate no guard electrodes, 1995 guard electrodes and wrap-around guard electrodes. From the figures, one can

see that both types of guard electrodes virtually eliminate the fringing fields around the end of the septum. Since the atom beam paths are very close to the septum, the elimination of the fringing fields, and hence uncertainty in  $E^2$  near the septum is advantageous for a precise measurement of polarizability. For this same reason, the phase gradient is more constant near the septum when it is protected by guard electrodes. The final grid for each plot is a  $1600 \times 1600$  square lattice of spacing  $62.5\mu\text{m}$ . Each plot was iterated at four different grid sizes of  $200 \times 200$ ,  $400 \times 400$ ,  $800 \times 800$  and  $1600 \times 1600$  nodes, for 40,000; 30,000; 10,000 and 10,000 iterations respectively. Using a 2.8GHz/1GB RAM PC, it took the 5-point averaging scheme about 24 hours to complete all three geometries, and it took the 9-point scheme about 48 hours.

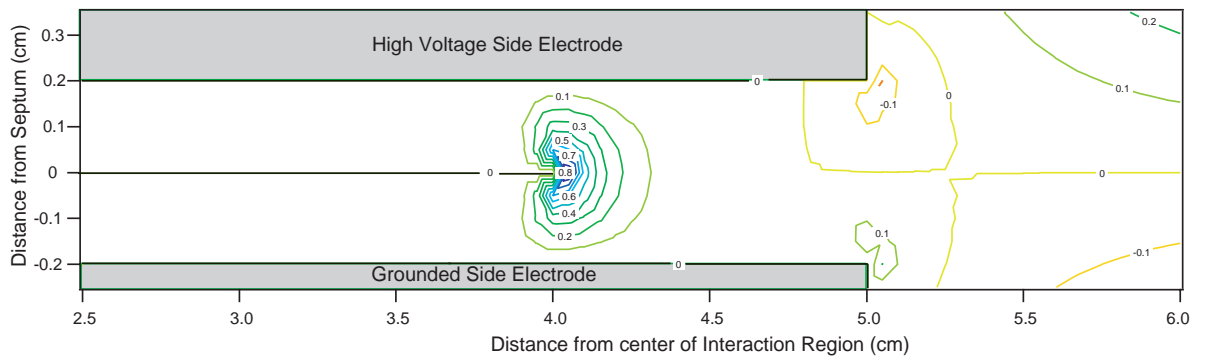


Figure 4.3: Difference plot of 5-point and 9-point scheme for no guard electrodes. The High Voltage Side Electrode is held at 1000V, and the Septum and Guard Electrodes are held at zero volts. The difference between the averaging schemes is shown in contours with spacing of 0.1V.

In the figures of the difference plots, the error also increases away from the end of the capacitor. The largest values for the difference between the averaging scheme Fig. 4.5 occurs at the right corners of the lattice. Therefore, I attribute this error between the schemes to the boundary conditions affecting one scheme differently than the other near the boundary. I believe the reason the potential difference in Fig. 4.5 is larger than Fig. 4.4 is because

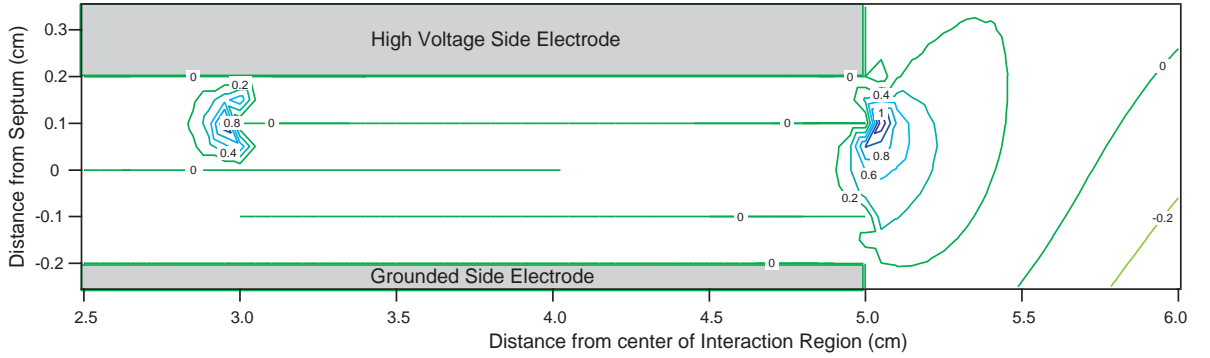


Figure 4.4: Difference plot of 5-point and 9-point scheme for 1995 guard electrode geometry.

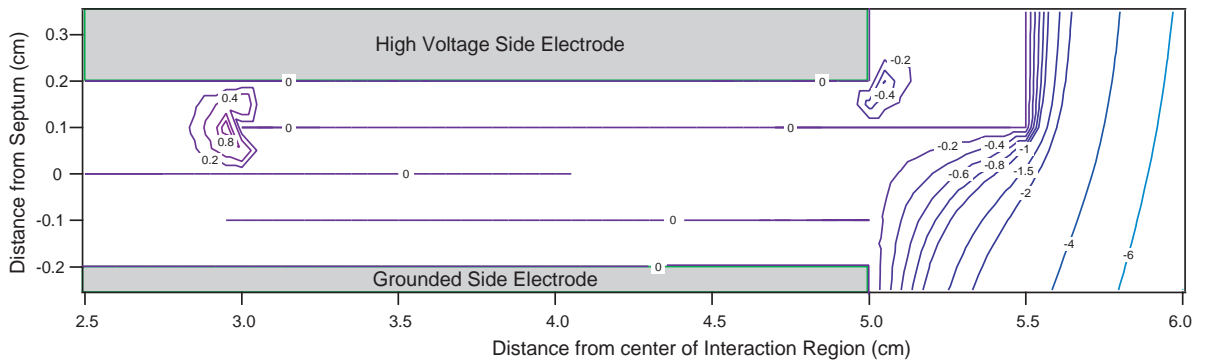


Figure 4.5: Difference plot of 5-point and 9-point scheme for wrap-around guard electrode geometry.

## 4.2 Calculating $\int \mathbf{E}^2 dz$

In this section, I will compare different methods to calculate the line integral,  $\int E^2 dz$ , along paths  $187.5\mu\text{m}$  on either side of the septum. I will also compare same line integrals for the 1995 guard electrodes and the wrap-around guard electrodes. The potential determined by the method of relaxation is used to calculate the electric field at each point along each path through the interaction region by

$$\int \mathbf{E}^2 dz = \int (E_x^2 + E_z^2) dz. \quad (4.8)$$

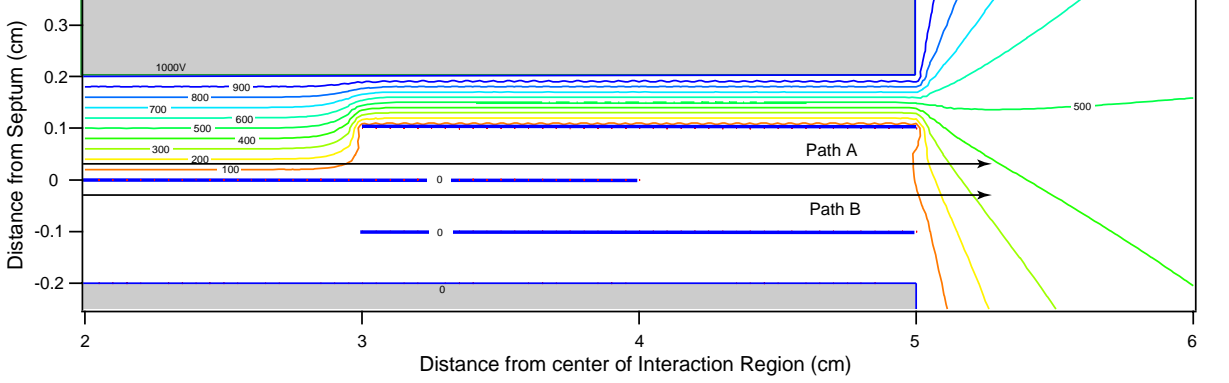


Figure 4.6: Potential plot of 1995 Geometry with original guard electrodes. Path A and B are  $187.5\mu\text{m}$  on either side of the septum. The wiggles in the 100 and 900V contour lines is an artifact of the graphing routine. The supporting structure for the guard electrode is modeled as free space.

The discrete first order derivative is used to calculate the components of electric field from the potential. This line integral, with limits  $z = -\infty$  and  $z = \infty$ , is used to determine  $L_{eff}$  for the paths through the interaction region. Two equations that determine the derivative at each point along the path, to varying accuracy, are

$$E_x = \frac{dV}{dx} = \frac{-V(x+2h) + V(x-2h) + 8V(x+h) - 8V(x-h)}{12h} + O(h^4) \quad (4.9)$$

and

$$E_x = \frac{dV}{dx} = \frac{V(x+h) - V(x-h)}{2h} + O(h^2). \quad (4.10)$$

Similar equations are written for  $E_z$ . Figures 4.6 and 4.7 show the potential found using the 5-point averaging method for both guard electrode types. The potential difference between the high voltage electrode and the septum is 1000V in both configurations. I calculated the line integral,  $\int_0^{10\text{cm}} \mathbf{E}^2 dz$ , using Eq. (4.9) and (4.10) for Path A and Path B. The line integrals and the percent difference between the schemes is listed in Tables 4.1 and 4.2. This shows that the derivative accurate to order  $O(h^2)$  is accurate enough under the conditions used in this example (primarily the grid spacing  $h=62.5\mu\text{m}$ ).

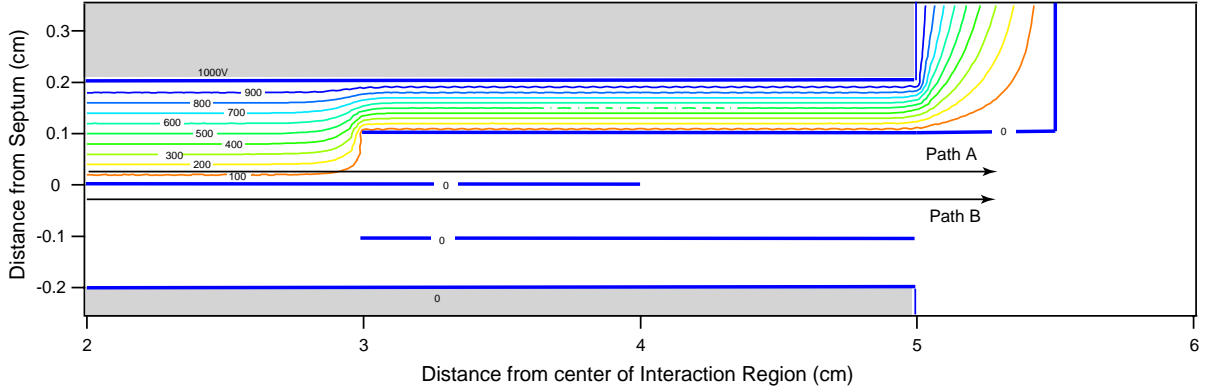


Figure 4.7: Potential plot of 1995 Geometry with wrap-around guard electrodes. Path A and B are  $187.5\mu\text{m}$  on either side of the septum. The wiggles in the 100 and 900V contour lines is an artifact of the graphing routine. The supporting structure for the guard electrode is modeled as free space.

Figures 4.8 and 4.9 show where along the line integral the electric field contribution is the largest. These graphs show that the wrap-around electrodes create an electric field outside the capacitor with a peak value three orders of magnitude smaller than with the original electrodes.

Increasing the node density in the averaging method for the electric field is always possible, but after certain point when the accuracy in  $\int \mathbf{E}^2 dz$  exceeds 0.01%, then the resources used in reducing the uncertainty due to numerical methods may be better used determining the error contributions due to the uncertainty in the geometric measurements. The uncertainty

Table 4.1: Line integrals,  $\int_0^{10\text{cm}} \mathbf{E}^2 dz$ , for original guard electrodes.

Path	$O(h^2)$ ( $\text{V}^2/\text{cm}$ )	$O(h^4)$ ( $\text{V}^2/\text{cm}$ )	% Diff.
A	48705488	48704299	0.002
B	813000	812788	0.011

Table 4.2: Line integrals,  $\int_0^{10\text{cm}} \mathbf{E}^2 dz$ , for wrap-around guard electrode geometry.

Path	$O(h^2)$ ( $\text{V}^2/\text{cm}$ )	$O(h^4)$ ( $\text{V}^2/\text{cm}$ )	% Diff.
A	47736868	47735587	0.003
B	5607.93	5607.94	0.0001

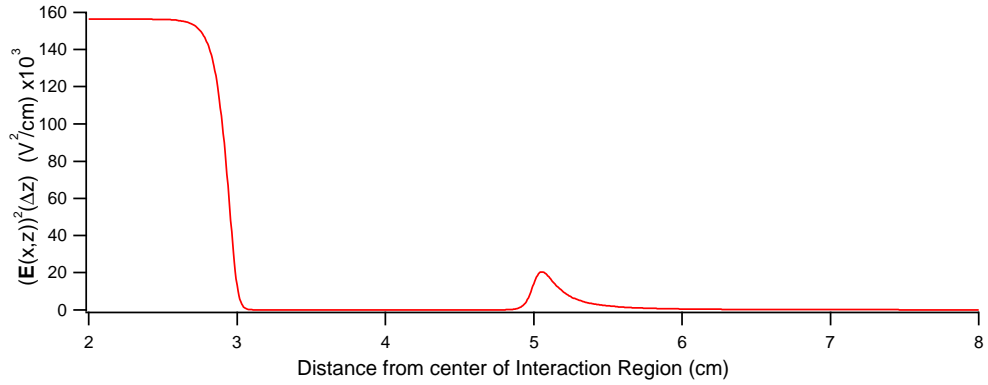
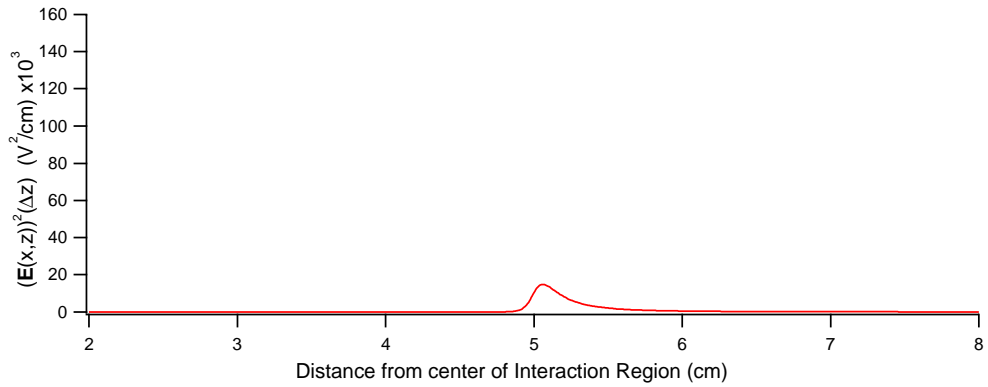
(a)  $\mathbf{E}^2 \Delta z$  as a function of position along Path A(b)  $\mathbf{E}^2 \Delta z$  as a function of position along Path B.

Figure 4.8: The 1995 Geometry with original guard electrodes.

in  $\int \mathbf{E}^2 dl$  due to geometry measurements that effect the field inside the capacitor make the uncertainty due to the numerical methods irrelevant.

When you are far enough inside the capacitor, the electric field is uniform, and when you are far enough outside the capacitor the field goes as  $\frac{1}{r^3}$  where  $r$  is the distance from the center of the capacitor. This dipole approximation for the field far outside the capacitor is an upper bound as the use of wrap-around guard electrodes will significantly reduce the magnitude of the electric field outside the capacitor by making the EFA have a quadrupole moment to leading order.

The line integrals we are interested in are closer to the septum than these examples. The use of guard electrodes (either type) significantly reduces fringing fields at the end of the septum.

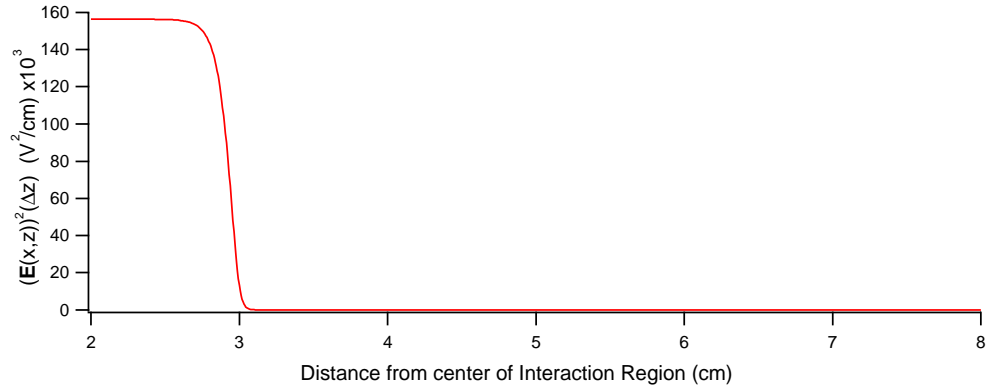
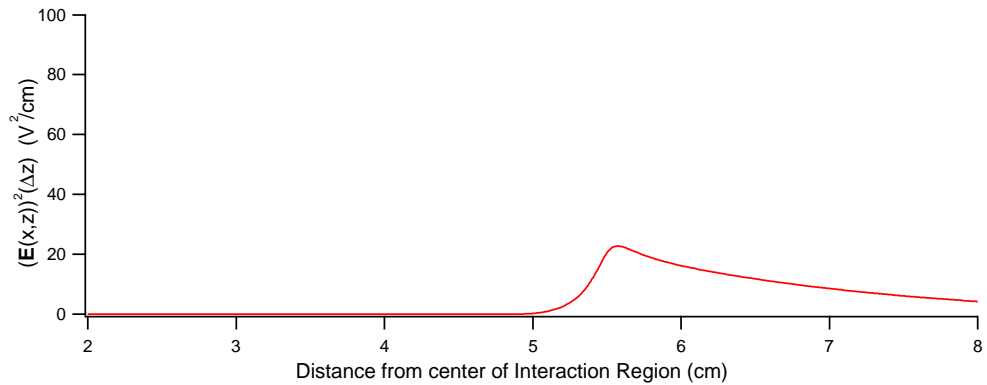
(a)  $\mathbf{E}^2 \Delta z$  as a function of position along Path A(b)  $\mathbf{E}^2 \Delta z$  as a function of position along Path B.

Figure 4.9: The 1995 Geometry with wrap-around guard electrodes. Note: the scale for the vertical axis is  $\sim 10^3$  smaller than (a).

Therefore, the paths pass through an area of the fringing field is small compared to the amount that is far enough inside or outside the capacitor. By reducing the fringing fields in the paths of the discrete line integral, I am reducing the amount of numerical error contributed to the line integral significantly.

Using these line integrals and the dipole approximation for far field (which provides a very conservative upper bound for the wrap-around guard electrodes), the amount of electric field inside and outside the interaction region can be determined. I defined the ends of the septum as the boundary for inside and outside. For the original guard electrodes, the difference between the integral  $\int_{-\infty}^{\infty} E^2 dl$  over Path A and Path B has a total contribution from the field outside the

interaction region of less than 0.25%. For the wrap-around guard electrodes, the contribution is less than 0.0004%.

The best method by which to determine the uncertainty in  $L_{eff}$ , is to calculate  $\int E^2 dl$  for the specific geometric measurements and repeat with small variations due to the uncertainty in those measurements. The geometric measurements necessary to include in this process are the length of the high voltage electrode  $L$ , the geometry and length of the guard electrodes, and the spacing between the guard electrodes and the septum. The uncertainty in the separation distance  $D$  contributes directly to the uncertainty in the polarizability.

### 4.3 Comparison to Semi-Infinite Capacitor

If there were an exact solution for the potential of a finite length capacitor, then we would be able to calculate the exact line integral for the paths of the arms of the interferometer. J. Cross [21] provides a solution to Laplace's equation which allows one to draw the potential lines for a semi-infinite parallel plate capacitor. It does not provide you with the equation for the potential, but the equations for the equipotential lines give the correct potential on the boundaries.

I modeled a finite length capacitor with a large length to separation ratio. The potential values for the numerical model corresponded exactly to those for the analytical solutions far inside the capacitor and on the line that bisects the capacitor. Outside the capacitor, the difference in the values increased farther from the bisecting line. For dense mesh plots, the direction that the equipotential lines shift in the finite length capacitor when compared to the same equipotential line in the semi-infinite capacitor is intuitively correct.

As you move away from the end of the capacitor, the effect of the boundary causes the potential contours to "bend" towards them so that they intersect normal to the boundary. The "bending" effect is illustrated in Fig. 4.10 where I plotted the entire range of the  $128 \times 128$  node mesh used to numerically solve for the potential around half parallel plate capacitor. Fig. 4.11 shows how using a more dense grid provides a more accurate solution for the potential that

the less dense grid. It also shows how the potential for either grid is more accurate closer to the horizontal bisecting line of the capacitor.

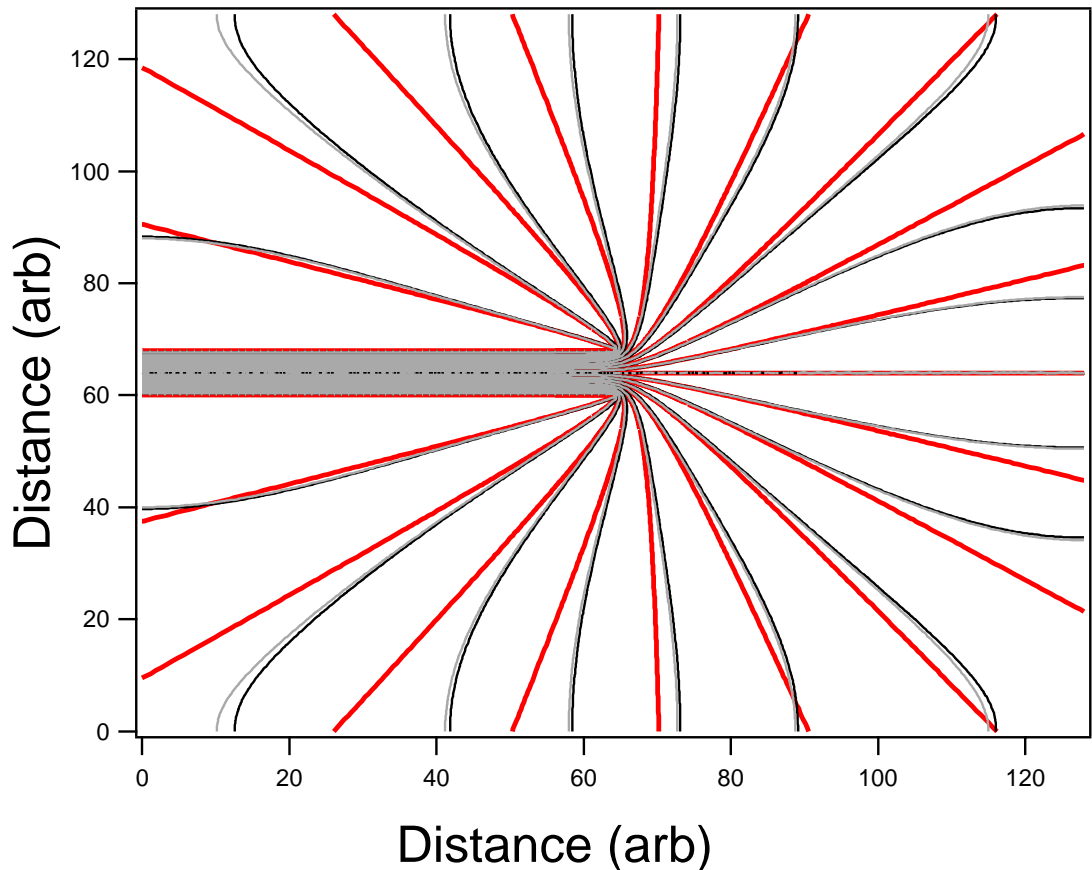


Figure 4.10: Comparison of an exact solution to a numerical calculation over the entire region modeled using the 5-point relaxation code. The two capacitor plates are held at  $+V$  and  $-V$ , spacing of contour lines in each set is  $0.1V$ . The left boundary uses the modified von Neumann boundary conditions. The other boundaries and corners use the simplest von Neumann boundary conditions. The thick lines are the potential lines for the semi-infinite capacitor analytical solution. The thin gray potential lines were determined with dense grid density that is 4 times as dense as the grid density used for the thin black lines. This figure is to show how the boundaries effect the potential lines near the boundaries

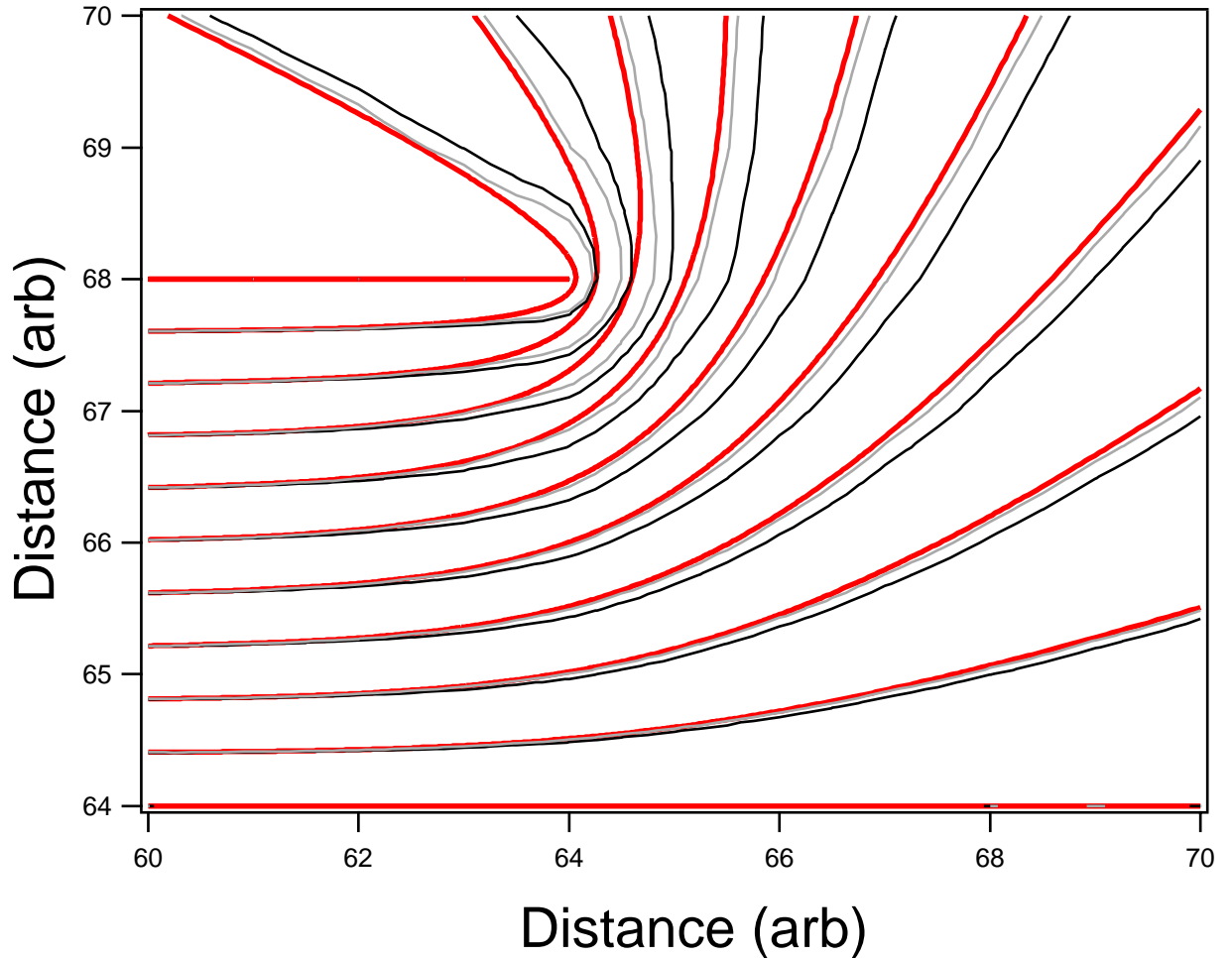


Figure 4.11: The region is the region modeled using the 5-point relaxation code. The thick lines are the exact potential lines for the semi-infinite capacitor. The thin gray potential lines were determined with dense grid density that is 4 times as dense as the grid density used for the thin black lines. This figure is to show that the more dense grid models the potential lines more accurately.

The potential points we are using to calculate the line integral are near the line that bisects the plates of the capacitor. Therefore, this check confirms that the model solves for a potential that is generally correct in the region that contributes the most to the line integral,  $\int \mathbf{E}^2 dl$ .

#### 4.4 The Algorithm of the FORTRAN Code

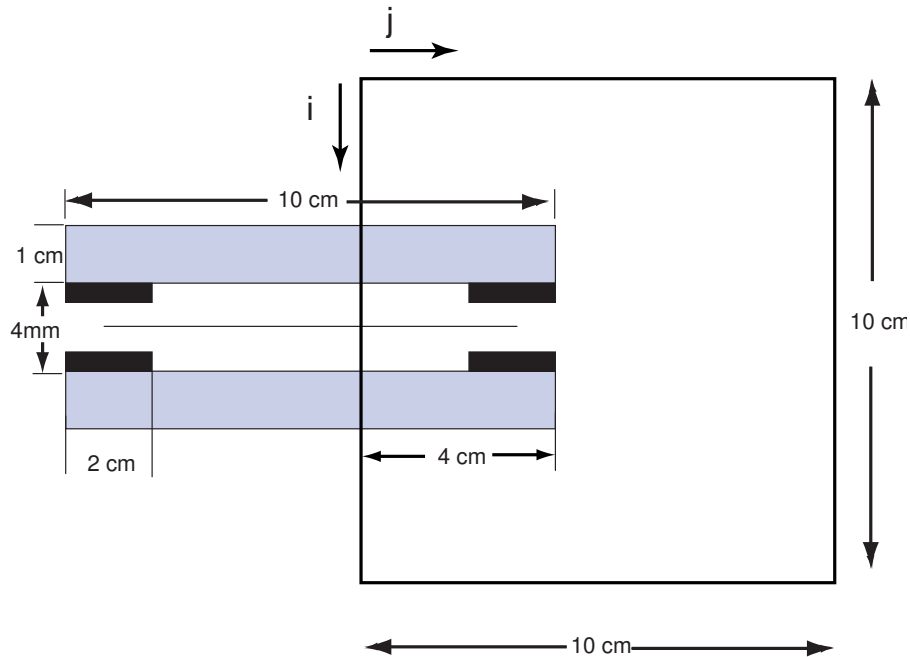


Figure 4.12: The region bounded by the large rectangle is the region modeled using the relaxation code. The left boundary uses the modified von Neumann boundary conditions. The other boundaries and corners use the simplest von Neumann boundary conditions.

Given the geometry of the EFA, I chose to use a rectangular mesh on which to model the apparatus and the potential. The reason for this is purely resource driven as I wanted to calculate the line integrals as close to the septum as possible. It is beneficial to plot the ratio  $L_{eff}/L$  for distances 5 to  $50\mu\text{m}$  away from the surface of the septum. Ideally, I would use a  $1\mu\text{m}$  or smaller square mesh, but the smallest rectangular mesh I was able to achieve, with 10 hours of computation time, was a  $6.25$  by  $62.5\mu\text{m}$  rectangular mesh which corresponds to grid points  $\frac{100\mu\text{m}}{2^4}$  and  $\frac{1000\mu\text{m}}{2^4}$ . The power of two in the denominator will be shown to be useful for determining the best initial guess values for the potential from a coarse grid. The grids used in the previous examples used a  $62.5\mu\text{m}$  square mesh, so I would conclude that the rectangular mesh used is at least as precise as the square grid for similar paths through

the interaction region. The only change with using a rectangular mesh is a few constants in deriving the averaging equation for the left boundary and the nodes throughout. I modeled the region shown in Fig. 4.12 that includes half of the capacitor. I chose to use the 5 point averaging method with a step size  $h$  in the  $i$  direction and  $k$  in the  $j$  direction where  $k = ah$ . For the rectangular grid, this method is accurate to fourth order in each step size,  $O(h^4, k^4)$ . I chose to use the 5-point averaging plan

I found the potential for points that are not on a boundary with the equation

$$V_{i,j} = \frac{1}{2 + 2a^2} (V_{i,j+ah} + V_{i,j-ah} + a^2 V_{i+h,j} + a^2 V_{i-h,j-1}) \quad (4.11)$$

where  $a$  is the ratio of step sizes.

There is a left-right symmetry to the geometry of the system that transfers to the equipotential lines and the electric field lines. Therefore, I chose to use the following averaging method for the boundary that nearly bisects the capacitor vertically,

$$V_{i,j} = \frac{1}{2 + 2a^2} (a^2 V_{i+h,j} + a^2 V_{i-h,j} + 2 \times V_{i,j+ah}). \quad (4.12)$$

This equation correctly determines the uniform electric field on the left boundary of Fig. 4.12 inside the capacitor.

For the other boundaries, I chose to use the simplest von Neumann boundary conditions which require the normal derivative to the boundary to be zero. For example, the averaging equation used to determine the value of the potential on the top boundary ( $i=0$ ) is [22]

$$V_{i=0,j} = V_{i+1,j}. \quad (4.13)$$

An example of the averaging equation for the upper right corner ( $i=0, j=\max$ ) is

$$V_{i,j} = V_{i+h,j-ah}. \quad (4.14)$$

The EFA is modeled to scale on a rectangular grid, and the grid density starts out very coarse with  $h = 100\mu\text{m}$  and  $k = 1000\mu\text{m}$ . In a  $10\text{cm} \times 10\text{cm}$  area, this means there are  $10^5$  nodes. All nodes are relaxed with each iteration. Each density is sufficiently relaxed through

numerous iterations. Through testing, this means at least one iteration per node for the initial grid density. This is an approximation because different geometries and locations on the grid require a different number of iterations to become fully relaxed. An accurate initial guess for the potential can greatly reduce the number of iterations necessary for the first grid density to become sufficiently relaxed. For example, using the 5-point averaging method a grid of 100,000 nodes, it takes about 2 hours to complete 100,000 iterations. Each time the node density quadruples, the number of iterations is reduced by a factor of four so the grid density takes the same amount of time to iterate each successive grid density. The first node density requires the most iterations because the initial guess at the potential is farthest from the true solution. Subsequent initial guesses are based on the results of the previous density. Because of this, subsequent node densities will require fewer iterations to become fully relaxed. To achieve the desired grid density of  $h=6.25\mu\text{m}$ , the grid density is doubled four times which is about 10 hours of computation time. To perform this same operation with the 9-point scheme would take approximately twice as long. You can see that increasing the number of iterations on subsequent grid densities, and/or going to larger grid density quickly makes this process time intensive. If the number of iterations is only reduced by 2 instead of 4 each subsequent grid density, the total time to complete the above example would increase to 62 hours.

## 4.5 Concluding Remarks on the Electric Field Model

Overall, I am confident that the model can calculate  $\int \mathbf{E}^2 dl$  to an accuracy of at least 0.01% for geometries using the wrap-around electrodes. I believe that the guard electrodes reduce the fringing fields along the paths the atoms take through the interaction region. The wrap-around electrode geometry makes the electric field outside the capacitor negligible which means it has little effect on the overall uncertainty of  $\int \mathbf{E}^2 dl$ . Uncertainties in the geometry that have an effect on the field inside the capacitor contribute significantly more to the uncertainty in  $\int \mathbf{E}^2 dl$ .

The rectangular grid will have more uncertainty than a square grid using the smaller step-size. But the final grid density for rectangular grid was  $h=6.25\mu\text{m}$  by  $ah=62.5\mu\text{m}$ . More

computing resources will be necessary to use a  $1\mu\text{m}$  square grid spacing over an equivalent region of space. I estimate the numerical uncertainty in  $\int \mathbf{E}^2 dl$  using the  $62.5\mu\text{m}$  square grid to be about 0.25%. By using a smaller grid size will allow this uncertainty to be reduced to about 0.05%.

## CHAPTER 5

# ELECTRIC FIELD APPARATUS

### 5.1 Overview

There were several important criteria taken into account when designing the improved EFA. The main criteria were that the two electrodes must be very flat and parallel, that the septum electrode must be very thin, and that the physical dimensions must be well known, specifically the separation distance and electrode lengths. I examined various materials, bonding techniques, and measurement techniques to optimize these criteria. The parallel plate capacitor is the general design idea for the EFA because it creates a uniform electric field for a large region of space.

I performed several tests to evaluate the quality of the construction for the prototype EFAs. The first test was to use a reflection-mode Fabry-Perot interferometer to evaluate the flatness of the septum. The second test was to place a voltage on the EFA and measure the changes in the separation distance of the electrodes by observing the interferogram. This test of applying voltage also provided measurement of the breakdown voltage in the EFA in air which is used as a lower bound for the breakdown voltage expected in vacuum.

Why use a parallel plate capacitor and not some other geometry that may provide a more precisely known but not uniform electric field? First, the two arms of the atom interferometer are separated by  $100\mu\text{m}$  which requires any electrode separating the two paths to be very flat. As described earlier, the line integral of electric field squared for the arm of the atom beam passing through the EFA is proportional to  $L_{eff}$ , which is one of the measured variables used to determine the polarizability, see Eq. (3.4). An ideal parallel plate capacitor would create a constant and uniform electric field for the atom beam to pass through. This electric field is accurately known up to the the surface of the electrodes. This reduces the need to know the exact path of the atom beam, because each path would pass through closer to the same

amount of electric field. The atom beam also has a certain amount of thickness, and, with an ideal parallel plate capacitor, all atoms in the beam would experience the same electric field. This means all the atoms get the same amount of phase shift. By using guard electrodes, a finite length parallel plate capacitor can be made to function very much like an ideal parallel plate capacitor for certain paths through the capacitor. It is for these reasons, I chose not to change from the original 1995 design of using a parallel plate capacitor.

## 5.2 Components of the Apparatus

I will describe several components of the electric field apparatus (EFA). For each component, I will describe how it contributes directly to the goal of creating a more precisely known electric field. The main components of the EFA are the septum electrode (SE), the high voltage electrode (HVE), the substrate, and the frame. The general diagram of the EFA and the orientation of the Fabry-Perot interferometer is shown in Fig. 5.1. A schematic showing the orientation of the interaction region inside the atom interferometer is shown in Fig. 5.2.

### 5.2.1 Septum Electrode (SE)

The material for the SE needs to have the following properties: thin, flat enough to resolve optical fringes, and able to be metalized. After testing several materials, ultra-thin silicon was chosen as the best material for the SE. Silicon is very strong and rigid, making it easy to manipulate. Its rigidity also allowed it to remain very flat during the assembly process. The SE is coated with gold to make it conducting. Silicon wafers are not a uniform thickness, but rather this thickness varies from 3 to 5  $\mu\text{m}$  depending on the manufacturer. This thickness variation limits how flat the silicon will be once it is mounted on the substrate. But it is flat enough to allow for variations to be seen with the laser interferometer. The silicon wafers used in the current assemblies were purchased from University Wafer in Massachusetts who manufacture them to a thickness of  $30 \pm 3 \mu\text{m}$ . Virginia Semiconductor makes wafers as thin as

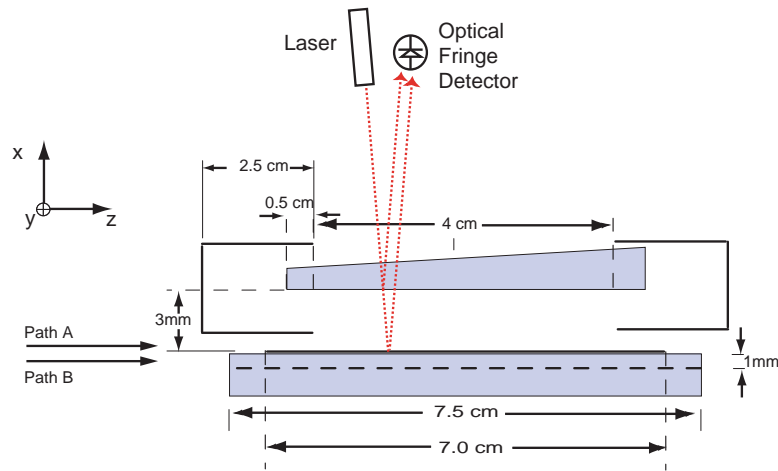


Figure 5.1: Details the geometry of the desired 2005 EFA viewed from above. The guard electrodes are shown to wrap around the HVE displayed as the wedged window. The silicon is represented by the dark line on the substrate which is the bottom rectangle. The supporting structures are not shown, but they are between the guard electrode and the septum. The other end of the guard electrodes are stabilized to the frame. The dashed line through the substrate represents the groove.

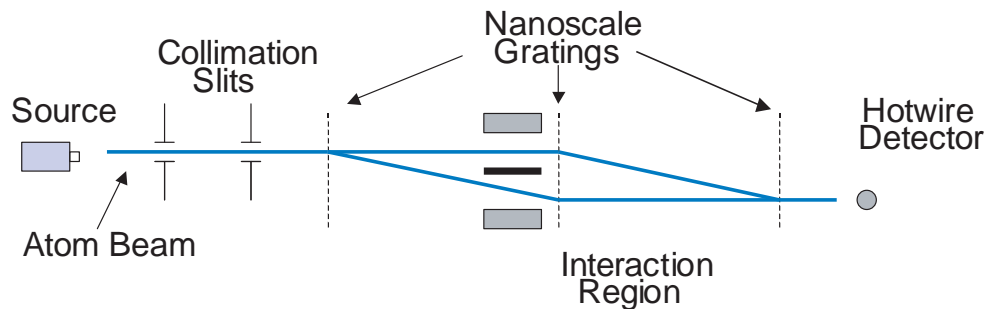


Figure 5.2: Diagram shows the position of the EFA inside the atom interferometer. The HVE is the top electrode of the interaction region. The silicon is the dark line between the arms of the interferometer.

$20 \pm 5 \mu\text{m}$ . Virginia Semiconductor also advertises wafers as thin as  $10 \mu\text{m}$  but the tolerance is not known.

If the silicon can be mounted flat except for this  $3 \mu\text{m}$  variation in thickness, then it would cast a thinner shadow for the atom beam than the metal foil used in previous designs [2].

The  $10\mu\text{m}$  metal foil used in previously built apparatuses was much thinner than the silicon, however the shadow cast by the septum due to imperfections was about  $20\text{-}30\mu\text{m}$ . Another advantage for choosing silicon is that it can be bonded to glass using a method known as anodic bonding.

Alternative materials were evaluated for possible use as the SE. Such materials included  $3$  and  $5\mu\text{m}$  copper foil and mica. Theoretically, because of its atomic structure mica could be cleaved to very thin planes; however, I was unable to cleave a suitable size slab of mica to thicknesses below about  $20\mu\text{m}$ . High quality (Grade V1)  $1\times 3\text{in}$  mica sheets, could be cleaved to between  $20$  and  $25\mu\text{m}$  thick, but at that thickness the surface varied greatly. Neither of these materials could match the flatness of silicon. By using the ultra thin foil and a technique to keep it under tension, it may be possible to create a very thin septum, but we have had most success in prototypes based on thin silicon wafers.

### 5.2.2 High Voltage Electrode (HVE)

The HVE is an optical grade wedged window. The window is lightly coated with gold to create a conducting beam splitter. The sputtered gold is on the order of  $10\text{nm}$  thick. The beam splitter property of the electrode enables a Fabry-Perot Interferometer to be set up between the HVE and the SE. The interference fringes allow the variations in the electrode separation to be measured.

### 5.2.3 Substrate

The requisite properties of the substrate are that it must be very flat and able to pass an atom beam on either side of the septum. The silicon is attached to a glass substrate so that it spans a groove. The “tunnel” formed allows the control arm to pass outside the high electric field region. In order to get the silicon to lay as flat as possible, the substrate itself must be flat. The groove cut into the substrate must not have any burrs protruding higher than the surface plane of the substrate. For these reasons, optical windows were chosen to be the substrate. When the glass or ceramic is cut, the material chips at the edge of the groove but

burs that protrude higher than the surface plane are rare. The flatter the substrate, the less it will contribute to the large scale surface deviations of the silicon. Materials considered that meet the above requirements were Pyrex and Zerodur glass. Corning Glass makes Pyrex, and Schott Glass makes Zerodur.

Anodic bonding was identified as a good way to attach the Si firmly to glass. This can result in an optically flat bond without glue, tape or other mechanical structures. As will be described, anodic bonding requires the joint be made at elevated temperatures, preferably between 250 and 300°C. Therefore, I searched for substrates that had a close match to the thermal coefficient of expansion for silicon. Silicon's thermal coefficient of expansion varies significantly as a function of temperature over the range of 30 to 500°C as shown in Fig. 5.3. In papers on anodic bonding, pyrex is recommended as a glass that would match silicon's expansion. By heating the glass and silicon sufficiently enough, the two materials expand equal amounts so that when they cool there is no fracturing or buckling of the septum electrode. Figure 5.3 shows that the critical temperature at which silicon will have expanded more than pyrex is about 180°C. At temperatures of greater than about 450°C the glass will have expanded more than the silicon. I have also included two other Corning glasses with slightly smaller and larger thermal coefficients of expansion and Zerodur for comparison. Through experiment, we found that heating to approximately 290°C, caused the silicon to bond to the pyrex at a point where the silicon has expanded more than the glass resulting in a very flat silicon surface across the groove in the substrate. At room temperature, the Si is kept under tension by this bond.

An alternative material for the substrate was aluminum. Aluminum is machined much easier than glass, but the uneven surface and burs on the edge of the groove prevented the silicon from laying flat. After machining several pieces of aluminum and attaching silicon with poor results, I concluded that the substrate must be optically flat to allow for an attached piece of thin silicon to be flat enough to resolve optical fringes.

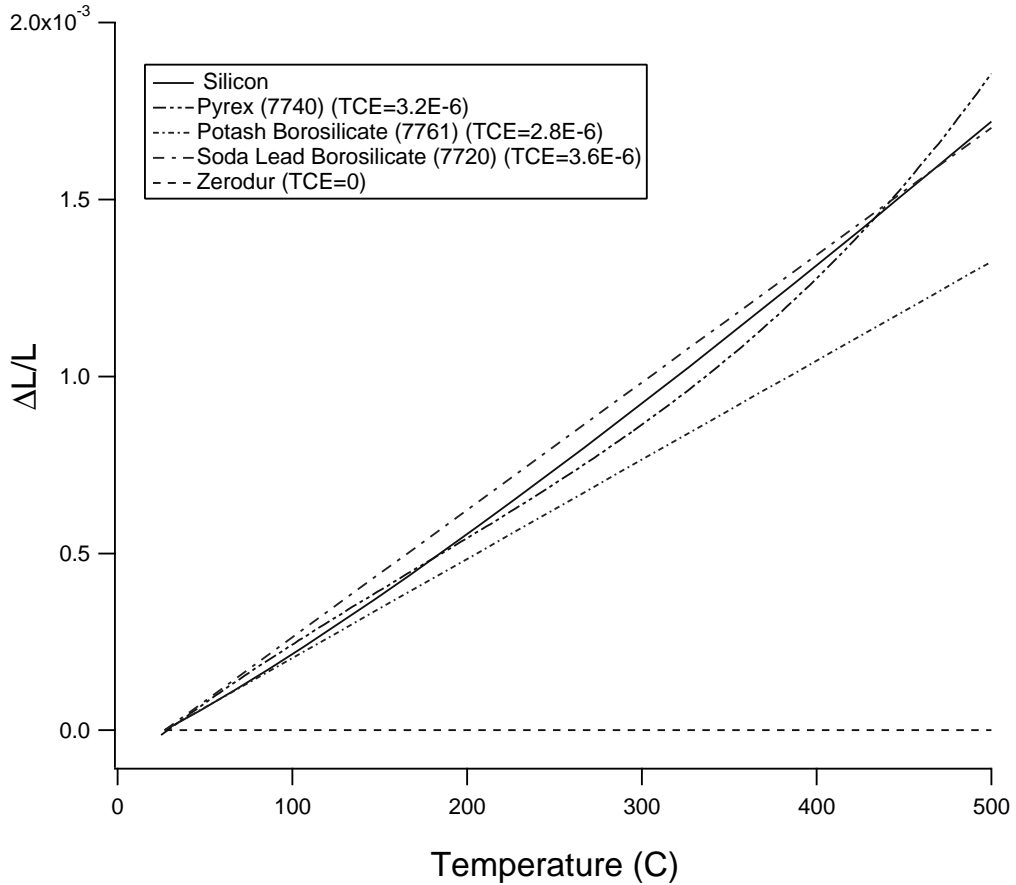


Figure 5.3: This plot compares the relative expansion for various possible substrates. Pyrex is the best choice for achieving a small amount of tension in the silicon at a desirable temperature for anodic bonding. TCE stands for temperature coefficient of expansion. I also included the Corning glass code for each glass type. I plotted the Si line using TCEs from R. B. Roberts [23]. I plotted the Pyrex using information from a Pyrex curve material properties pamphlet [24].

#### 5.2.4 Frame, Spacers and Guard Electrodes

The frame contains degrees of freedom that allow for alignment of the HVE and SE, as well as adjustment of  $D$ . I use the same precision spacer to initially establish  $D$ . I measured the spacers using the same technique as Ekstrom [2] and achieved similar results. The separation distance between the SE and the guard electrodes requires a spacer that is not as precisely known. I use 1/32in copper-clad circuit boards for these spacers. The guard electrode itself is

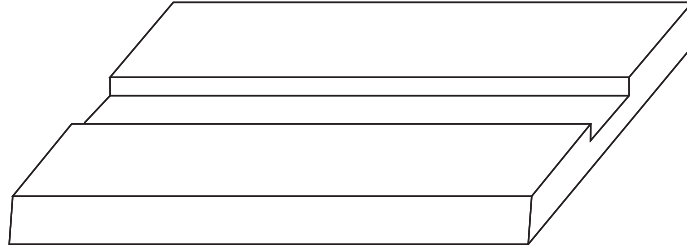


Figure 5.4: Diagram showing approximate scale of the groove to the substrate

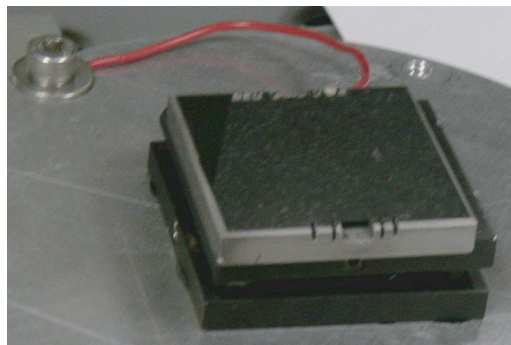


Figure 5.5: Photograph of 2in by 2in square pyrex with silicon bonded to the surface. The main groove and side grooves are visible.

made out of 0.005in copper-clad circuit boards. The part of the guard electrode that wraps around the HVE is made out of a metal foil.

### 5.3 Assembling the EFA

The process of assembling the EFA requires that great care is taken to ensure precise alignment. The primary groove in the substrate is cut, and narrower grooves are cut on either side of the primary groove to allow air to escape from under the silicon. Perhaps the most critical in the process, is to attach the SE to the substrate so that it is flat across the groove. The method anodic bonding was selected as the best option to accomplish this task. Other methods including wax, epoxy at room temperature, epoxy at 0 °C, and tape provided less desirable results. A common theme of the epoxy and wax was that while in liquid form, the adhesive would flow under the silicon causing the silicon surface to be warped once it hardened. Anodic bonding does not require any foreign substance to be placed between the silicon and

substrate to complete the bond. In fact, foreign substances between the silicon and substrate would prevent the silicon from laying flat. Anodic bonding of silicon to glass was originally

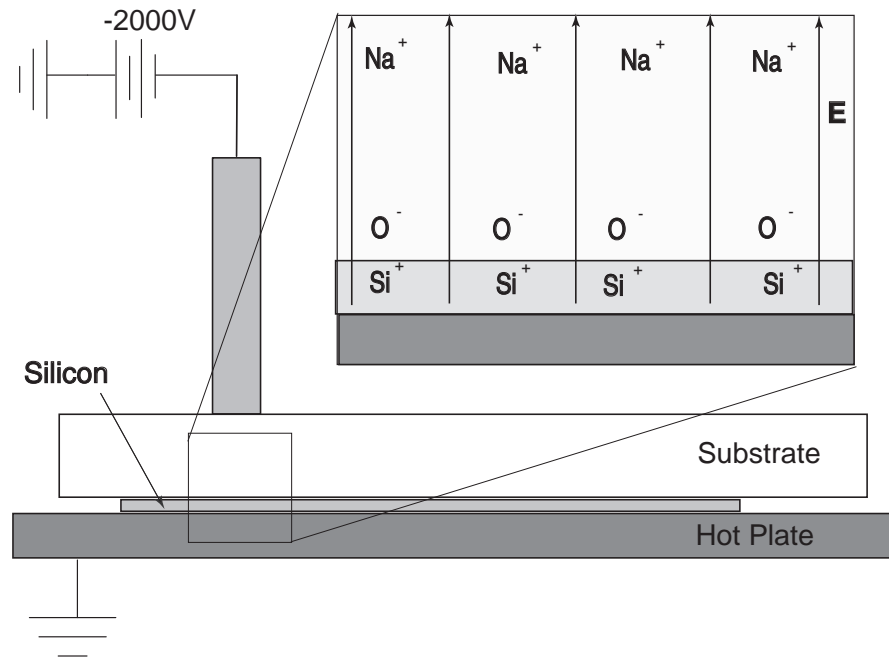


Figure 5.6: Diagram illustrates the general setup for bonding the silicon to the substrate.

developed in 1969 [25]. It involves heating the glass and silicon to make the ions more mobile and then applying a strong electric field as shown in Fig. 5.6. The result is a thin layer of silicon oxide that forms between the glass and silicon. This layer permanently bonds the silicon to the glass.

Prior to bonding the silicon to the substrate, the main groove and about 1mm on either side of the groove is metalized. This shields that portion of the silicon from the electric field. This allows the silicon to bond, but it prevents the silicon from bonding in the small chips on the edge of the groove. Once the silicon is attached to the substrate, that portion of the EFA is metalized. When this part of the EFA is held at ground, the control arm will be entirely shielded from the electric field created by the HVE. Of course, any fringing fields the control arm encounters will still have an effect on the atoms.

The guard electrodes are attached to the SE using epoxy. Their separation defines the true length,  $L$ , of the the capacitor. The guard electrodes shield the end of the SE from high electric fields, but also reduce the length of the capacitor by at least 1cm.

The HVE and SE are aligned so that the surfaces are as parallel as possible. A spacer of known thickness is attached to the substrate so that  $D$  can be set to this spacer thickness.  $D$  can then be increased to the desired amount.

Photographs of an EFA built with wrap-around guard electrodes is shown in Fig. 5.7. A close-up, side view of the main groove and septum is shown in Fig 5.8. A picture that shows the surface of the septum and the guard electrodes is in Fig. 5.9.

## 5.4 Critical Geometric Measurements

Absolute measurements of  $D$  and  $L$  are important for an independent measurement of a polarizability. In Chapter 6, I discuss the use of a ratio measurement to eliminate the uncertainty due to the geometry of the EFA.

### 5.4.1 Separation of the Electrodes

Measuring the separation of the electrodes,  $D$ , is critical for a precise determination of the electric field. One initial goal of this research is to achieve an accurate measurement of the separation to less than a wavelength of light. This goal was not achieved, several possible methods are explained in this section.

#### 5.4.1.1 Laser Interferometer Techniques

Several techniques were investigated to determine the absolute separation distance between the two electrodes. The first is to have a system where the electrodes are aligned so that they are parallel. The electrodes are brought together and then separated slowly a desired amount. While the electrodes separate, the number of fringes could be counted and the total separation distance could be determined to a quarter the wavelength of the light. This method was tested

with an interferometer using a HeNe laser. Fringe data from tests of this method are shown in Fig. 5.10.

Another technique may involve using several lasers of different frequencies. By comparing the fringe data from the different sources, one may be able to measure the separation distance with a similar method as above, but without having to start with the plates at zero separation.

#### 5.4.1.2 Fabry-Perot Optical Interference Fringe Pattern

An absolute measurement of the separation distance of the electrodes using light interferometry was not accomplished. However, a method using a Fabry-Perot interferometer to create interference fringe data did allow us to monitor any variations in the separation distance  $D$ . The fringe pattern of the EFA is monitored in situ and variations to the separation distance as the voltage is applied can be monitored. A sample fringe pattern from a prototype is shown in Fig. 5.11.

The interference fringe data could be used to assist in determining separation  $D$  with greater relative uncertainty. A precisely known 2mm spacer is attached to the substrate such that lies flush with the silicon wafer.  $D$  is adjusted so the HVE touches the spacer.  $D$  is then increased from this point to the desired amount. The change in  $D$  is measured by counting the number of fringes that pass a given point. This allows for larger separation distances to be known to an absolute error of about  $1.5\mu\text{m}$ .

#### 5.4.2 Length of the High Voltage Electrode

The other critical length measurement is the length  $L$ , which is the length between the guard electrodes and defines the length of the HVE. We can measure  $L$  to an accuracy of  $25\mu\text{m}$  for lengths of 5 to 10 cm using a caliper. It would be desirable to make the HVE as long as 10cm. By using a precision spacer instead of a caliper, the uncertainty in the length of  $L$  could be reduced. I used several gauge blocks as the precision spacer. These gauge blocks are small enough to be measured with the caliper accurate to  $1\mu\text{m}$ .

When the wrap-around guard electrodes are used, the length of the septum electrode is such that it be at 2cm longer than the HVE so that sufficient overlap with the guard electrode can be achieved. See Fig. 5.1, for the geometry of the of the EFA that I designed.

#### 5.4.2.1 Contributions to the Uncertainty in $L$

I will now discuss two alignment uncertainties which use the coordinate system defined in Fig. 5.1. First, the zeroth order arm is aligned so as to be as parallel to the septum as possible. There will be uncertainty in this alignment in both the z-x and z-y planes. Given the length of the apparatus, the distance between the guard electrode and the septum and the width of the groove, the largest angle between the beam and the septum is less than  $0.6^\circ$ . The additional length of  $L$  due to misalignment of the atom beam is determined using

$$\Delta L = L \left( \frac{1}{\cos\theta} - 1 \right), \quad (5.1)$$

where  $L$  is the length between the guard electrodes and  $\theta$  is the angle between the atom beam and the septum electrode. If  $\theta$  is  $0.6^\circ$  and  $L$  is 4cm then  $\Delta L$  is  $2\mu\text{m}$ .

The previous uncertainty treats the atom beam as a perfectly collimated beam which is not necessarily the case. The each arm has a cross section that is about  $20\mu\text{m}$  wide and  $500\mu\text{m}$  high. Worst case, some atoms may leave the source at the top of the beam and hit the detector at the bottom of the beam. Since the width is much smaller than the height, I will neglect it for these calculations. Given that the interferometer is about 3m long from source to detector, the maximum angle for an atom to have is less than  $0.01^\circ$ . Using Eq. 5.1, this corresponds to a  $\Delta L$  of less than  $6\text{\AA}$ .

## 5.5 Evaluation of a Prototype

As described before, the separation  $D$  is created by touching the HVE to the 2mm spacer and then backing it away a set number of fringes. For a 3mm spacing, the relative uncertainty in  $D$  would be about 0.06%. I was not able to conduct this measurement, but was able to test the ability to measure relative distances using fringe data.

Measurement of the spacing of the guard electrode to the HVE. Using the three largest gauge blocks as a precise 4cm spacer the guard electrodes were measured to be 4cm apart with an uncertainty of less than  $25\mu\text{m}$ . The sizes of the gauge blocks are 1.0002cm, 1.5004cm and 2.5004cm with each having an uncertainty of 0.0002cm. Using combinations of these blocks as the spacer for the guard electrodes, a length  $L$  can be made that is  $4.0008\pm 0.0004\text{cm}$ . I will add an uncertainty of  $25\mu\text{m}$  due to aligning the zeroth order arm so that it is parallel with the septum electrode. This is an estimation based on the 1995 error calculation. Since the zeroth-order arm is made parallel to the septum, the first-order arm is definitely not parallel to the septum. However, using wrap-around guard electrodes the first-order arm passes through no electric field inside the capacitor so this additional distance the arm travels inside the capacitor has no effect. The length of the SE was measured with an uncertainty of  $25\mu\text{m}$ .

### 5.5.1 Breakdown Voltage

I tested the amount the distance  $D$  varied as the voltage was increased for a septum that spanned a 1cm main groove. No changes in the interferogram were observed until the voltage was over about 2.5kV at which time I could observe the fringes moving. I observed the fringes move a distance that corresponded to a decrease in the distance  $D$  of about 150nm before the capacitor shorted in air at about 2.7kV.

The support structure used in the current design does have any spacers wedged between the HVE and the SE. This removes the regions where breakdown commonly occurs; along the edge of the spacer. Figure 5.12 illustrates the two types of support structures.

### 5.5.2 Determining $L_{eff}/L$

I determined the ratio  $L_{eff}/L$  using the model discussed in Chapt. 4. I compared the phase gradient for the 1995 geometry with original guard electrodes to the phase gradient for the 2005 geometry with wrap-around guard electrodes. Figure 5.13 compares  $L_{eff}/L$  as a function of distance from the septum (which is proportional to the phase gradient) for the 1995 geometry and the 2005 geometry. The magnitude is questionable because the number of iterations needs

to be increased and the grid step size needs to be reduced to  $1\mu\text{m}$  or less. Because both plots were made using the same model, I believe that the slope of the line accurately shows that the wrap-around guard electrodes reduce the phase gradient on the zero-field side of the septum to zero. The wrap-around guard electrodes also reduce the phase gradient on the electric field side of the septum. The values in Fig. 5.13(a) do not match the values reported by Ekstrom, et. al. [2] exactly, but the slope of the line on each side of the septum corresponds well. This discrepancy between my model and [2] is

$$\left. \frac{L_{eff}}{L} \right|_{MyModel} - \left. \frac{L_{eff}}{L} \right|_{[2]Model} = |0.98160 - 0.98155| = 0.00005 \quad (5.2)$$

at  $x=20\mu\text{m}$  from the surface of the septum on the electric field side, and the discrepancy is

$$\left. \frac{L_{eff}}{L} \right|_{MyModel} - \left. \frac{L_{eff}}{L} \right|_{[2]Model} = |0.01515 - 0.01050| = 0.00465 \quad (5.3)$$

at  $x=20\mu\text{m}$  from the surface of the septum on the zero field side.

I estimated the numerical uncertainty could be reduced to about 0.05% by using a smaller grid size. I considered three other contributions to the uncertainty in  $L_{eff}/L$  for the EFA shown in Fig. 5.1: 1. the change in  $L_{eff}/L$  across the width of the beam ( $25\mu\text{m}$ ), 2. the spacing between the guard electrode and the septum electrode, 3. the length of the guard electrode, and 4. the length of the septum electrode. The uncertainty due to  $L_{eff}$  changing across the width of the beam is determined using Fig. 5.13(b) to be about 0.01%. An uncertainty in the spacing between the guard electrodes and the septum electrode of 0.13% corresponds to an uncertainty in  $L_{eff}/L$  of 0.03%. I determined that the length of the guard electrode and septum electrode could vary by as much as 0.1cm and the  $L_{eff}/L$  plot was unchanged.

I estimate the total geometric uncertainty for the 2005 geometry can be reduced to a contribution of 0.14% in  $\alpha$ . This is about a 25% improvement over the geometric uncertainty in the 1995 experiment. The geometric uncertainties are listed in Table 5.1.

### 5.5.3 Calculated Phase Shift

The designed 2005 EFA should create a phase shift of over 202 radians for a Na beam. The values used to calculate this potential phase shift for Na are as follows: length  $L$  is 4 cm,

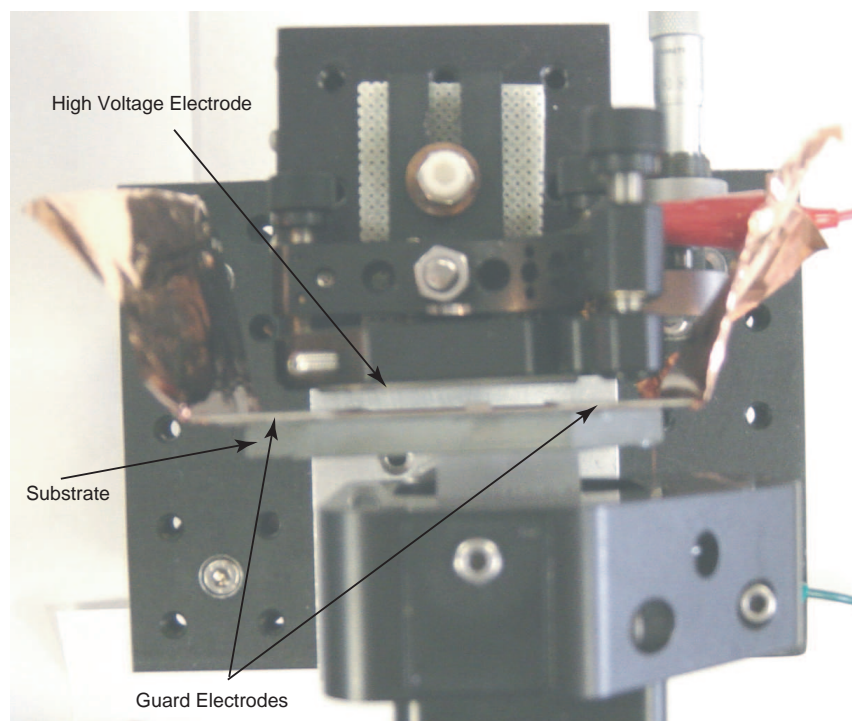
Table 5.1: Relative contributions of geometric error sources to the measured polarizability for the 2005 EFA.

Error Source	Systematic Error in $\alpha$
Spacer width, $D$ ( $3.0\text{mm}\pm 1.5\mu\text{m}$ )	0.06%
Interaction region length, $L$ ( $4.0008\text{cm}\pm 4\mu\text{m}$ )	0.06%
Electric field calculation correction ( $L_{eff}/L$ )	0.06% <sup>1</sup>

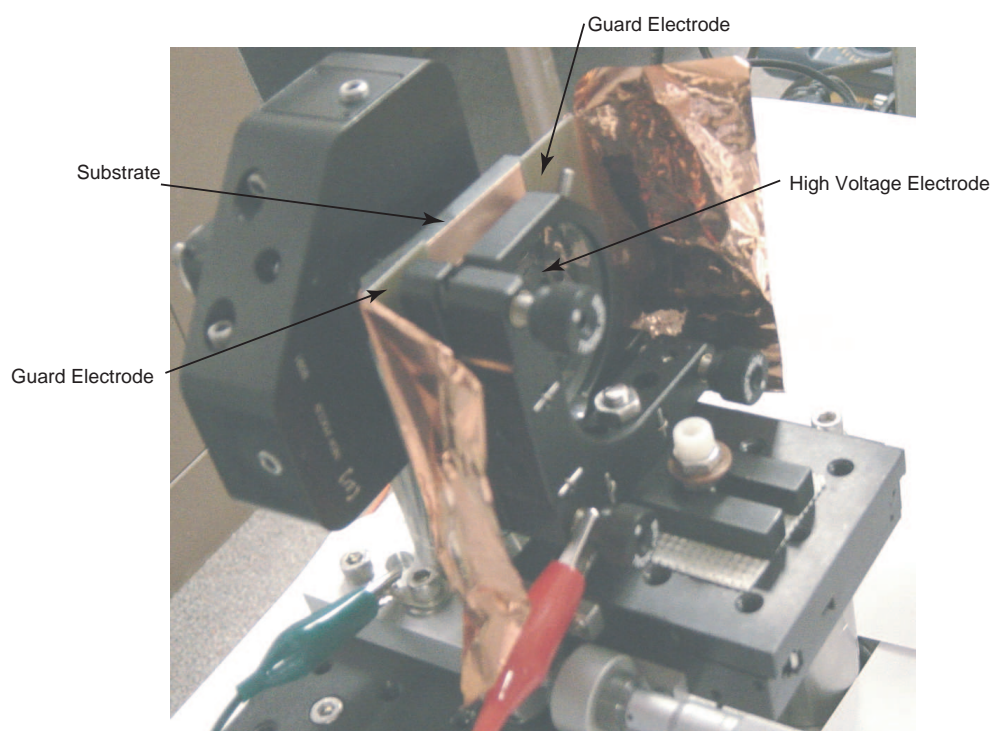
the separation distance  $D$  is 0.3cm, and the voltage difference is 2kV, atom beam velocity of  $1\times 10^5\text{cm/s}$ , a polarizability of  $24.11\times 10^{-24}\text{cm}^3$  and that the  $L_{eff}$  is about 94% of the total length  $L$ .

---

<sup>1</sup>This value assumes an uncertainty due to the averaging method of less than 0.05% which should be achievable by using a step size of  $1\mu\text{m}$  or less and paths within  $50\mu\text{m}$  of the septum.



(a) EFA prototype top view



(b) EFA prototype oblique angle view

Figure 5.7: 2005 Electric Field Apparatus prototype pictures.

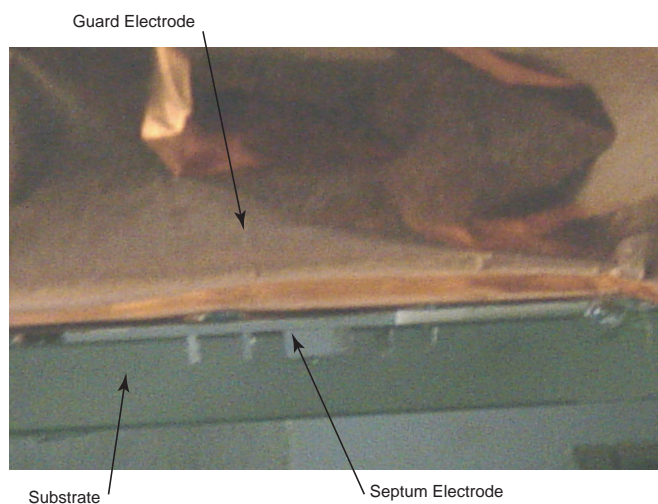


Figure 5.8: Picture of the prototype from the side. This provides a good view of the main groove, side grooves, and the silicon septum that spans the groove. The general path of the atom beam is into or out of the page.

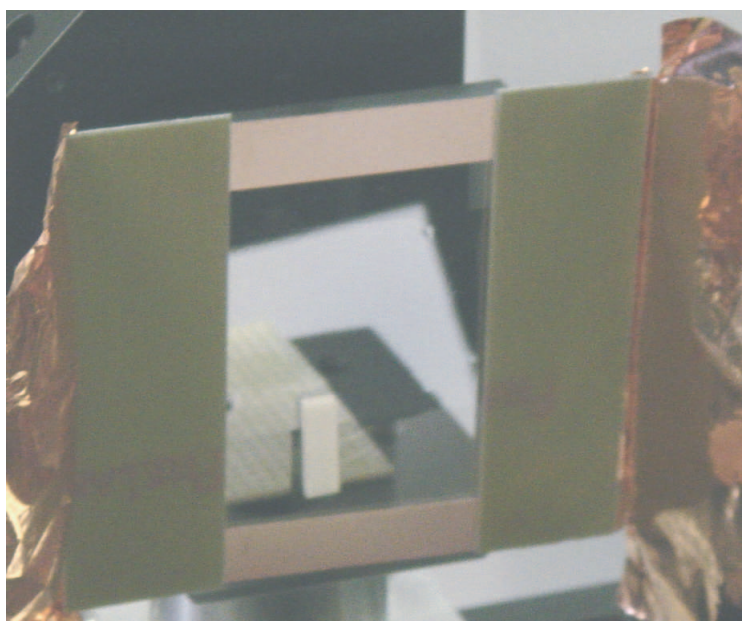
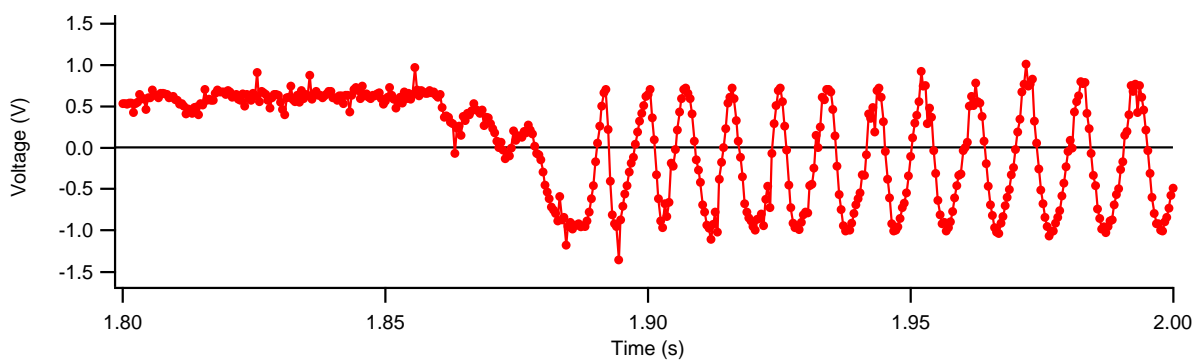
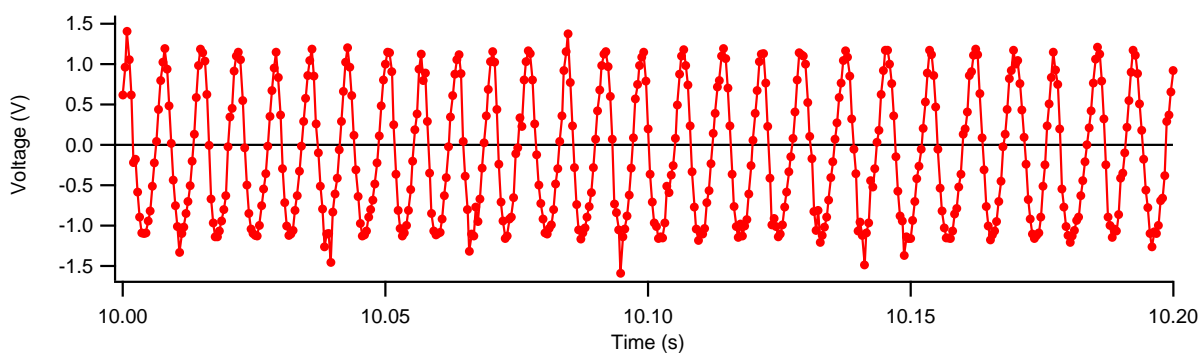


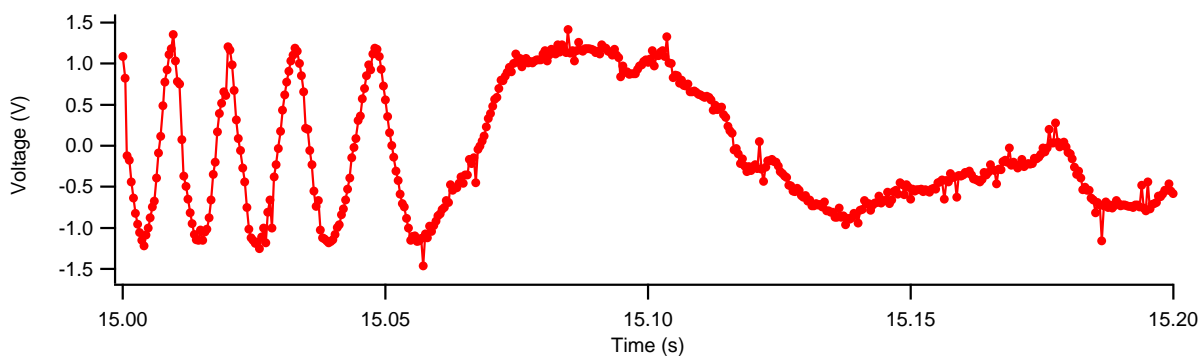
Figure 5.9: Picture of the prototype septum surface and guard electrodes.



(a) Initial separation of electrodes. Not exactly a uniform fringe at first due to fact that the electrodes are not perfectly parallel when they are in contact.

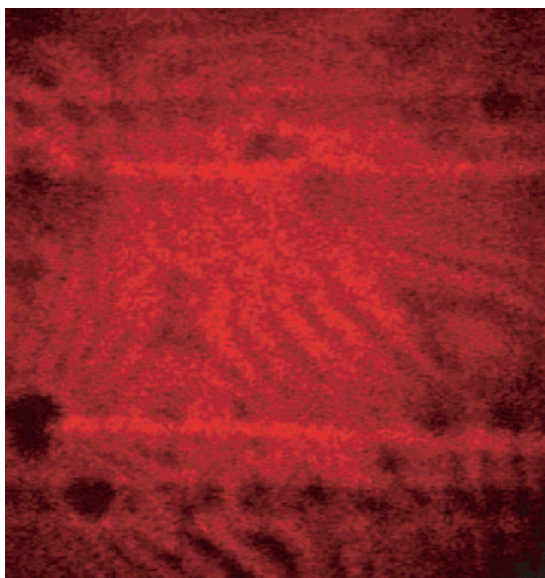


(b) Section of fringe data while electrodes are separating at a constant rate.

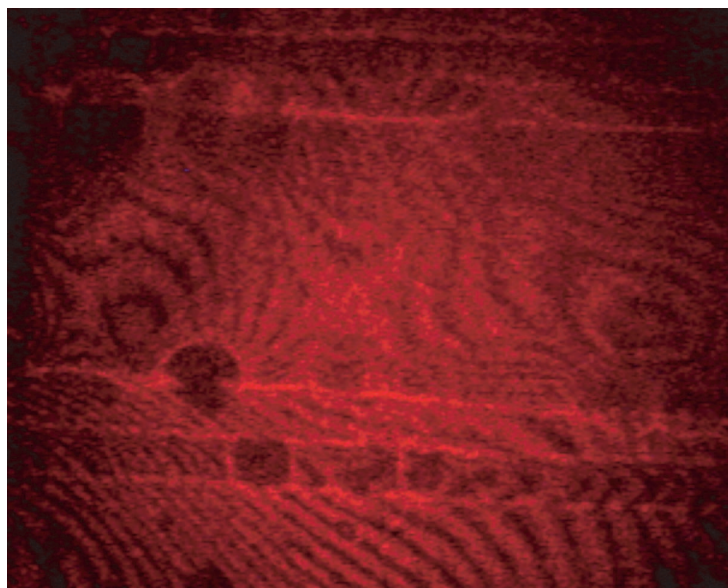


(c) Data when electrodes stop moving. It is evident that the motor does not stop instantly and that there could be some oscillation about the point at which electrodes stop moving.

Figure 5.10: Fringe data for two plates separating from contact.



(a) Sample Interaction Region Interferogram

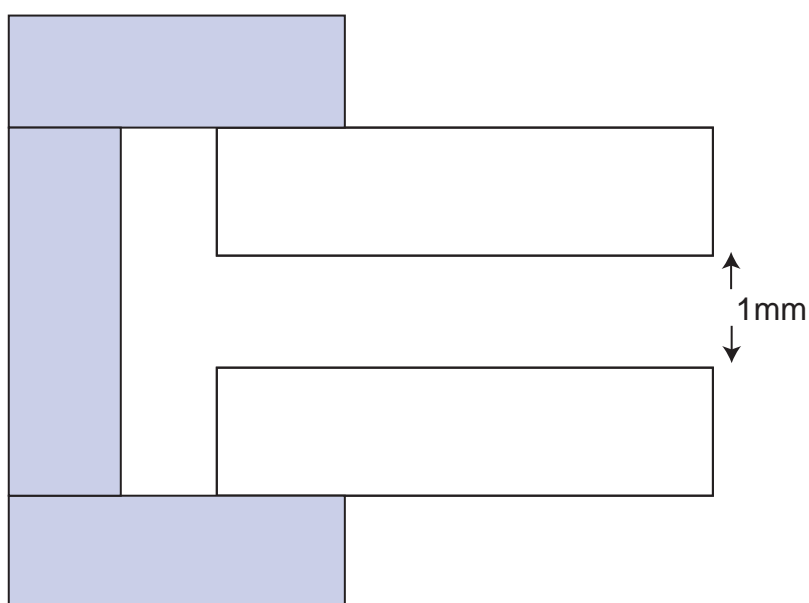


(b) Sample Interaction Region Interferogram

Figure 5.11: Fringe patterns using 632.8nm laser light. Both (a) and (b) are made using the same septum.



(a) Support structure with spacer wedged between the electrodes.



(b) Support structure using an external frame.

Figure 5.12: The plots show two possible configurations to hold the two electrodes a fixed distance from each other. In (a), along the edge of the spacer is the place where breakdown will occur first as the potential difference between the plates is increased. By removing this pathway with configuration (b), a higher potential difference between the plates can be achieved before breakdown.

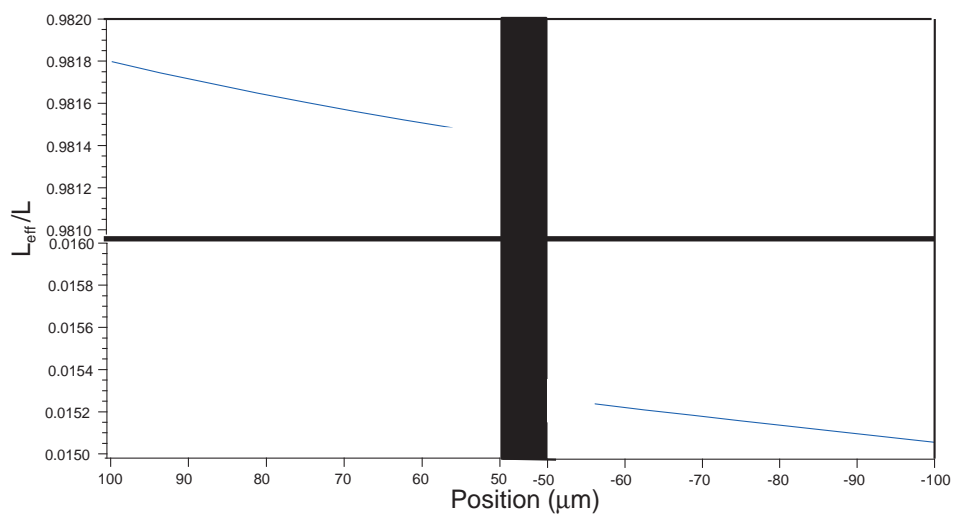
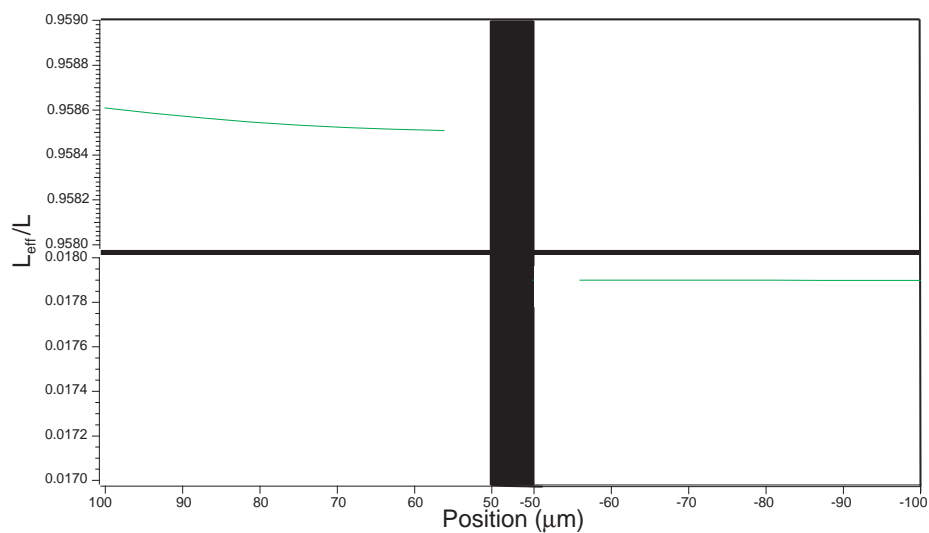
(a) 1995 Electric Field Apparatus  $L/L_{eff}$ (b) 2005 Electric Field Apparatus  $L/L_{eff}$ 

Figure 5.13: The plots show that the wrap-around guard electrodes used in the 2005 EFA reduce the the  $L/L_{eff}$  gradient on both sides of the septum. The septum is the dark vertical line in the center.

## CHAPTER 6

### PERFORMING A RATIO MEASUREMENT

A ratio measurement is discussed in detail in T. D. Roberts Ph.D. thesis [20]. In a very precise ratio measurement, each species of atom must travel the same path through the electric field side of the interaction region. The thickness of the septum limits the ability to measure heavier atoms. The polarizability of each atom species is determined using the equation

$$\alpha = \left( \frac{\Delta\phi}{V^2} \right) \left( \frac{D^2}{L_{eff}} \right) (2\hbar v). \quad (6.1)$$

It is evident that when two species of atoms are taken using the same interaction region, the geometric quantities and the associated uncertainties are equivalent. The resulting equation looks like

$$\frac{\alpha_1}{\alpha_2} = \left( \frac{\Delta\phi_1}{\Delta\phi_2} \right) \left( \frac{v_1}{v_2} \right) \quad (6.2)$$

and shows the ratio polarizability measurement is dependent on the ratio of the phase difference. The uncertainty in the velocity can be reduced with the dispersion compensation technique.

The separation in the arms of the interferometer is dependent on the deBroglie wavelength of the atom species and the geometries in the atom interferometer. The separation  $w$  can be determined by

$$w = \frac{\lambda_{dB}}{t} L_{grating} \quad (6.3)$$

where  $t$  is the period of the gratings and  $L_{grating}$  is the spacing between the first two gratings. For the current atom interferometer  $t=100\text{nm}$  and  $L_{grating}=1\text{m}$ . The velocity of the atom beam is controlled by the carrier gas and can have any velocity between about 700m/s (using Xenon) and 3000m/s (using He). For a Cs beam, with 100nm period gratings and a 1000m/s beam, the maximum separation of the arms is about  $30\mu\text{m}$ . With a 700m/s carrier gas, this increases to about  $43\mu\text{m}$ . Therefore, with a thin septum it may be possible measure the polarizability of Cs using the atom interferometer.

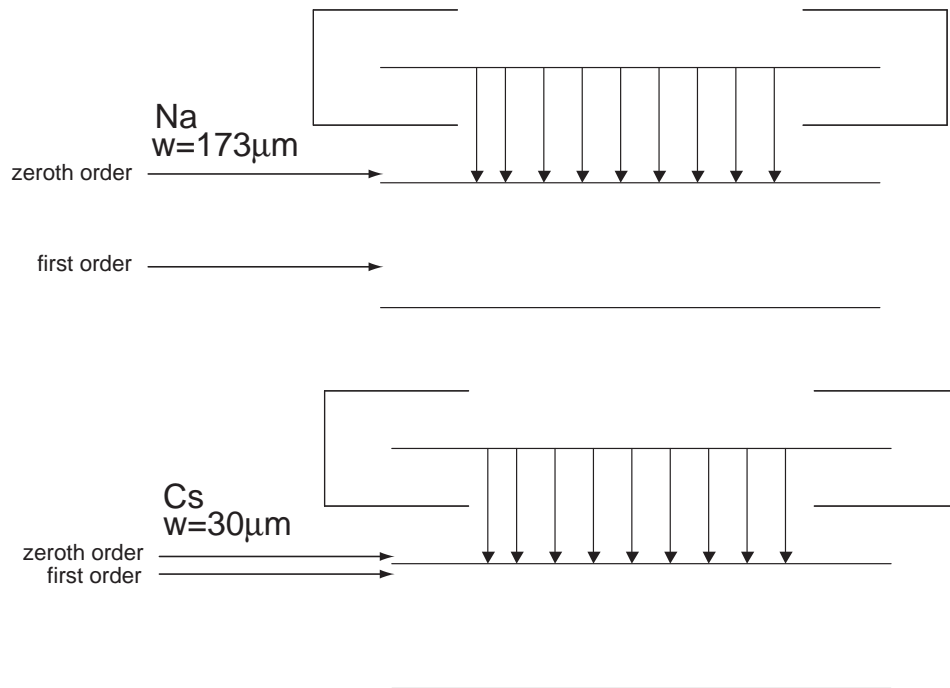


Figure 6.1: This figure shows how the negligible phase gradient on the zero field side of the septum allows atom beams of different species to be aligned along the same path through the electric field. For the current atom beam, a Na source would have a separation of about  $173 \mu\text{m}$ , and a Cs source would have a separation of about  $30 \mu\text{m}$ . The value  $w$  is the separation of the interferometer arms at the second grating. The first-order arm is not parallel to the zeroth order, but the arm passing on the zero field side need not be parallel to the septum.

The 2005 EFA design nearly eliminates the electric field seen by the arm that passes on the zero side of the septum. This ability makes sending different species of atoms along the same path through the electric field a more viable option. Regardless of the separation of the arms (as long as there sufficient separation for the septum), each species could be aligned to take the same path through the interaction region. The arm passing on the zero-field side of the septum will take different paths for each species with no adverse affect. Figure 6.1 illustrates this principle.

Using similar principles to that for a ratio measurement, calibration techniques could be used to accurately measure the separation distance  $D$  using an atom with a well known polarizability such as Li. Measurements could be taken for different distances of  $D$ . The optical fringe pattern

would be monitored closely so as to know the separation distance variations to within one fringe. From these measurements, the separation distance could be determined for one of the measurements. From that information, the separation distance could be known for measuring the polarizability of other atoms.

## CHAPTER 7

### SUMMARY

In summary, I have successfully created a septum electrode using  $30\mu\text{m}$  silicon and characterized the surface using laser interferometry. These same techniques could be used with  $10\mu\text{m}$  silicon. The geometry of the EFA is such that it will create a phase shift between the arms of the interferometer in excess of 200 radians. Using numerical methods, I tested and showed that using wrap-around guard electrodes, the phase gradient in the arm on the zero-field side of the septum is negligible and the phase gradient in the arm on the field side of the septum is slightly less when compared to previous guard electrode configurations.

## CHAPTER 8

### FUTURE WORK

There were several areas of research that warrant further research, and will be necessary to complete in order to make the ratio measurement a reality.

#### 8.1 EFA

To improve the EFA, we must use  $\leq 10\mu\text{m}$  thick silicon wafers as the septum. If it is not possible to purchase 3 inch silicon wafers at the desired thickness, then it may be possible to use a preferential etch to make a silicon septum thinner.

We must build an EFA with largest  $L$  possible. This would increase the phase shift as well as reduce the relative uncertainty in  $L$ . It would also reduce the uncertainty in  $L_{eff}$  because field well known field inside the interaction region would contribute a larger percentage to the line integral  $\int \mathbf{E}^2 dz$ .

#### 8.2 Electric Field Modeling Program

Reduce grid size to a one micron grid without sacrificing the size of the region modeled. The F77 program may have been the limiting factor as to the maximum possible grid size. Processing time may be reduced by providing a better initial guess for the wrap-around guard electrodes. The interferogram provides useful information on how  $D$  varies as a function of  $z$  which could be incorporated into a model using  $\leq 1\mu\text{m}$  grid size.

Model only the field inside the electric field apparatus. Using the wrap-around guard electrodes, the field outside contributes a negligible amount to the line integral. The boundary conditions of such a model would all be correctly modeled using Dirichlet and Neumann conditions. In this manner, the grid step size could be reduced to one micron or less. Figure 8.1

illustrates the new placement of the relaxation grid boundary with respect to the 2005 EFA design.

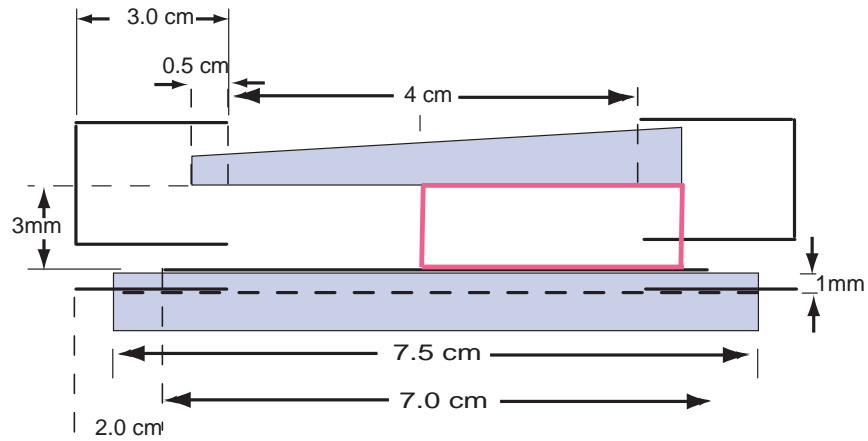


Figure 8.1: This figure shows the recommended placement of the relaxation grid boundary (red rectangle). The boundaries that fall on the electrode surface use Dirichlet conditions. The left and upper right boundary will correctly use Neumann conditions. The lower right boundary is approximated as having Dirichlet boundary conditions with a value of zero volts.

## Appendix A

### Sample FORTAN 5-point Scheme Rectangular Grid Code

```

program rectgrid1995geometry
integer i, j, iter, maxi, maxj, max_iter, n, s
integer xrange, yrange, maxn
double precision v1, v2, v3, v4, ex, ey, ee, ideal, unit
double precision alpha, epsi, hbar, vel, line, a
double precision d, L, G, SE, totee, fee
real potential(0:32100,0:3300)
real pot_old(0:32100,0:3300)
real pot_olda(0:32100,0:3300)

c ***unit is grid unit in i direction (transverse)

c ***a isscale factor for j direction (longitudinal)

c ***unitj = a*unit c ***s is the scale factor

c ***G is length groove in glass(plus guard electrode)

c ***SE is lenth of silicon septum

c ***L is length of +V electrode

      open (unit=25, file="testpot1", status="unknown")
      open (unit=24, file="testpot0", status="unknown")
      open (unit=22, file="firstgridsampn5", status="unknown")
      open (unit=21, file="firstgridsampn4", status="unknown")
      open (unit=19, file="pthaintn5", status="unknown")
      open (unit=18, file="pathintn4", status="unknown")
      open (unit=17, file="pthaintn3", status="unknown")
      open (unit=16, file="pathintn2", status="unknown")
      open (unit=15, file="pathintn1", status="unknown")
      open (unit=14, file="pathintn0", status="unknown")
      open (unit=12, file="ee", status="unknown")
      open (unit=11, file="testfirst", status="unknown")
v1 = 1000
v2 = 0

c *****Assume 1995 Geometry with guard electrodes

c (septum and guard electrode thickness of 100um)

      a = 10

```

```

L = 40
SE = 30
  G = 40
  xrange = 1000
  yrange = 100

c Use cgs units for all values to get polarizability in cm^3

c Use potential in statvolts = 1 statvolt = 299.79 volts to

c calculate line integral if calculating phase

c All length units in cm

c Put hbar in correct units of erg s

alpha = 24.11E-24
epsi = 0.000000000008854188
hbar = 1.05456E-27
vel = 100000
d = .2
unit = .01
maxn = 4

c          start iterations over n

c          set size if grid for given n
do n= 0,maxn
s=2**n
maxi = xrange*s
  maxj = yrange*s

c          set number of iterations for each n

if (n==0) then
  max_iter = 200000
  write (*,*) "running n=0"
elseif (n==1) then
  max_iter = 50000
  write (*,*) "running n=1"
elseif (n==2) then
  max_iter = 12500
  write (*,*) "running n=2"
elseif (n==3) then
  max_iter = 3125
  write (*,*) "running n=3"
elseif (n==4) then
  max_iter = 782
  write (*,*) "running n=4"
elseif (n==5) then
  max_iter = 1

```

```

        write (*,*) "running n=5"
elseif (n==6) then
    max_iter = 1
    write (*,*) "running n=6"
endif

c          initialize starting potential of grid
if (n==0) then
    do i= 0, maxi
    do j= 0, maxj
c          potential(i,j) = V1/2
          pot_old(i,j) = V1/2
    enddo
    enddo

    else
    do i=0 , maxi
    do j=0 , maxj
        pot_olda(i*2,j*2) = pot_old(i,j)
        pot_olda((i*2)+1,2*j) = (pot_old(i,j) + pot_old(i+1,j))/2
        pot_olda(2*i,(j*2)+1) = (pot_old(i,j) + pot_old(i,(j+1)))/2
        pot_olda(2*i+1,j*2+1)=(pot_old(i,j)+pot_old(i,j+1)+pot_old(i+1,j)+pot_old(i+1,j+1))/4

    enddo
    enddo

    endif

c          set intermediate potential = pot_old
if (n>0) then
do i=0,maxi
do j=0,maxj
    pot_old(i,j) = pot_olda(i,j)

enddo
enddo
endif

c          write potential to file to check grid
if (n==1) then
c          write (*,*) "made it to here"
do i=0 , maxi
do j=0 , maxj
    write (11,*) i,j, pot_old(i,j)
enddo
enddo
endif

do iter=1 , max_iter

c          set electrode voltages at begining and after new grid guess
do j = 0,L*s

```

```

        pot_old((xrange/2-20)*s,j) = v1
        pot_old((xrange/2-120)*s,j) = v1
        pot_old((xrange/2 + 21)*s,j) = v2
        pot_old((xrange/2 + 121)*s,j) = v2
    enddo
do i = ((xrange/2-120)*s),((xrange/2-20)*s)
    pot_old(i,L*s) = v1
enddo

    do i = ((xrange/2+20)*s),((xrange/2+120)*s)
        pot_old(i,L*s) = v2
    enddo

do j = (L-20)*s,L*s
    pot_old((xrange/2 - 10)*s,j) = v2
    pot_old((xrange/2 - 11)*s,j) = v2
    pot_old((xrange/2 + 11)*s,j) = v2
    pot_old((xrange/2 + 12)*s,j) = v2
enddo

do x = ((xrange/2-11)*s),((xrange/2-10)*s)
    pot_old(i,(L-10)*s) = v2
    pot_old(i,(L)*s) = v2
enddo

do x = ((xrange/2+11)*s),((xrange/2+12)*s)
    pot_old(i,(L-10)*s) = v2
    pot_old(i,(L)*s) = v2
enddo

do j = 0,SE*s
    pot_old((xrange/2)*s,j) = v2
    pot_old((xrange/2+1)*s,j) = v2
enddo
do x = ((xrange/2)*s),((xrange/2+1)*s)
    pot_old(i,SE*s) = v2
enddo

do i=0 , maxi
do j=0 , maxj
c    ***RECTANGLE AVERAGING SCHEME (to order (h,ah)**2

c ***deal with edge of grid and corners

        if (i==0) then
potential(i,j) = pot_old(i+1,j)

                elseif(i==maxi) then

potential(i,j) = pot_old(i-1,j)

```

```

        elseif(j==0) then
potential(i,j) = 2*pot_old(i,j+1)
potential(i,j) = potential(i,j) + (a**2)*pot_old(i-1,j)
potential(i,j) = potential(i,j) + (a**2)*pot_old(i+1,j)
potential(i,j) = potential(i,j)/(2+2*(a**2))

        elseif(j==maxj) then
potential(i,j) = pot_old(i,j-1)

        else
c      ***do the averaging (5 point scheme) for rectangle grid

potential(i,j) = (a**2)*pot_old(i+1,j)
potential(i,j) = potential(i,j) + (a**2)*pot_old(i-1,j)
potential(i,j) = potential(i,j) + pot_old(i,j+1)
potential(i,j) = potential(i,j) + pot_old(i,j-1)
potential(i,j) = potential(i,j)/(2+2*(a**2))
        endif

        if(i==0)then
        if (j==0) then
c      potential(i,j) = (pot_old(i+1,j)+ 2*pot_old(i,j+1))/3
potential(i,j) = pot_old(i+1,j+1)
        endif
        endif

        if(i==0) then
        if (j==maxj) then
c      potential(i,j) = (pot_old(i+1,j)+ pot_old(i,j-1))/2
potential(i,j) = pot_old(i+1,j-1)
        endif
        endif

        if(i==maxi) then
        if(j==0) then
c      potential(i,j) = (pot_old(i-1,j)+ 2*pot_old(i,j+1))/3
potential(i,j) = pot_old(i-1,j+1)
        endif
        endif

        if(i==maxi) then
        if(j==maxj) then
c      potential(i,j) = (pot_old(i-1,j)+ pot_old(i,j-1))/2
potential(i,j) = pot_old(i-1,j-1)
        endif
        endif

        enddo
        enddo

c      ***make pot_old equal to potential

```

```

do i=0 , maxi
do j=0 , maxj
    pot_old(i,j) = potential(i,j)
enddo
enddo

c    ***end the do loop over iter within a specific n
enddo

c    ***set electrode voltages at for Pot_old for new n

do j = 0,L*s
    pot_old((xrange/2-20)*s,j) = v1
    pot_old((xrange/2-120)*s,j) = v1
    pot_old((xrange/2 + 21)*s,j) = v2
    pot_old((xrange/2 + 121)*s,j) = v2
enddo
do i = ((xrange/2-120)*s),((xrange/2-20)*s)
    pot_old(i,L*s) = v1
enddo

do i = ((xrange/2+20)*s),((xrange/2+120)*s)
    pot_old(i,L*s) = v2
enddo

do j = (L-20)*s,L*s
    pot_old((xrange/2 - 10)*s,j) = v2
    pot_old((xrange/2 - 11)*s,j) = v2
    pot_old((xrange/2 + 11)*s,j) = v2
    pot_old((xrange/2 + 12)*s,j) = v2
enddo

do x = ((xrange/2-11)*s),((xrange/2-10)*s)
    pot_old(i,(L-10)*s) = v2
    pot_old(i,(L)*s) = v2
enddo

do x = ((xrange/2+11)*s),((xrange/2+12)*s)
    pot_old(i,(L-10)*s) = v2
    pot_old(i,(L)*s) = v2
enddo

do j = 0,SE*s
    pot_old((xrange/2)*s,j) = v2
    pot_old((xrange/2+1)*s,j) = v2
enddo
do x = ((xrange/2)*s),((xrange/2+1)*s)
    pot_old(i,SE*s) = v2
enddo

```

```

c   ***INSERT LINE INTEGRAL CALCULATION HERE*****

c   ***use pot_old(i,j) as it just update and electrodes rewritten

c   ***calculate line integral of E**2 same for each n*****

c   ***derivative accurate to (h,ah)**2

        write (*,*) "Calculating Line Integrals."

        do i= ((xrange/2-7)*s),((xrange/2+8)*s)
            fee = 0
        do j=1 , maxj-1

            ex=pot_old(i+1,j)-pot_old(i-1,j)
            ex=(ex)/(2*unit/s)
            ey=pot_old(i,j+1)-pot_old(i,j-1)
            ey=(ey)/(2*(a*unit)/s)
            fee=fee+((ex**2 + ey**2)*((a*unit)/s))
c       write (*,*) fee
            enddo

c   ** Write to different file for each n  INSIDE i do loop*****
        if (n==0) then

            write (14,*) i, fee

        elseif (n==1) then

            write (15,*) i, fee

        elseif (n==2) then

            write (16,*) i, fee

        elseif (n==3) then

            write (17,*) i, fee

        elseif (n==4) then

            write (18,*) i, fee

        elseif (n==5) then

            write (19,*) i, fee
        endif
c   *****end i do loop for line integrals of E**2
        enddo

        Write to potential file for n=4

```

```

        if (n==4) then
do i=0 , (maxi/16)
do j=0 , (maxj/16)
write (21,*) i,j, pot_old(16*i,16*j)
enddo
enddo
endif

c          end do loop over n
enddo

c  ***reset electrodes to correct value for potential(i,j) array

do j = 0,L*s
potential((xrange/2-20)*s,j) = v1
potential((xrange/2-120)*s,j) = v1
potential((xrange/2 + 21)*s,j) = v2
potential((xrange/2 + 121)*s,j) = v2
enddo
do i = ((xrange/2-120)*s),((xrange/2-20)*s)
potential(i,L*s) = v1
enddo

do i = ((xrange/2+20)*s),((xrange/2+120)*s)
potential(i,L*s) = v2
enddo

do j = (L-20)*s,L*s
potential((xrange/2 - 10)*s,j) = v2
potential((xrange/2 - 11)*s,j) = v2
potential((xrange/2 + 11)*s,j) = v2
potential((xrange/2 + 12)*s,j) = v2
enddo

do x = ((xrange/2-11)*s),((xrange/2-10)*s)
potential(i,(L-10)*s) = v2
potential(i,(L)*s) = v2
enddo

do x = ((xrange/2+11)*s),((xrange/2+12)*s)
potential(i,(L-10)*s) = v2
potential(i,(L)*s) = v2
enddo

do j = 0,SE*s
potential((xrange/2)*s,j) = v2
potential((xrange/2+1)*s,j) = v2
enddo
do x = ((xrange/2)*s),((xrange/2+1)*s)
potential(i,SE*s) = v2
enddo

```

```
c          write potential to file (sample)
do i=0 , (maxi/s)
do j=0 , (maxj/s)
    write (22,*) i,j, potential(s*i,s*j)
enddo
enddo

c      do i=0 , maxi

c      do j=0 , maxj

c      write (22,*) i,j, potential(i,j)

c      enddo

c      enddo

end
```

## Appendix B

### FORTRAN 9-point Averaging Scheme

c Note: I used two additional matrices to do the 9 point averaging  
c method

c do the averaging (9 point scheme)

```

potc(i,j) = pot_old(i+1,j)/epsilon(i+1,j)
potc(i,j) = potc(i,j) + pot_old(i-1,j)/epsilon(i-1,j)
potc(i,j) = potc(i,j) + pot_old(i,j+1)/epsilon(i,j+1)
potc(i,j) = potc(i,j) + pot_old(i,j-1)/epsilon(i,j-1)
potc(i,j) = potc(i,j)*epsilon(i,j)/4

```

```

potx(i,j) = pot_old(i+1,j+1)/epsilon(i+1,j+1)
potx(i,j) = potx(i,j) + pot_old(i-1,j+1)/epsilon(i-1,j+1)
potx(i,j) = potx(i,j) + pot_old(i+1,j-1)/epsilon(i+1,j-1)
potx(i,j) = potx(i,j) + pot_old(i-1,j-1)/epsilon(i-1,j-1)
potx(i,j) = potx(i,j)*epsilon(i,j)/4

```

```

potential(i,j)=potx(i,j)/5+ 4*potc(i,j)/5

```

## REFERENCES

- [1] T. M. Miller and B. Bederson. Atomic and molecular polarizabilities - a review of recent advances. *Advances in Atomic and Molecular Physics*, 13:1–55, 1977.
- [2] C.R. Ekstrom, J. Schiedmayer, M.S. Chapman, T.D. Hammond, and D.E. Pritchard. Measurement of the electric polarizability of sodium with an atom interferometer. *Phys. Rev. A*, 51(5):3883–3888, May 1995.
- [3] P. Berman, editor. *Atom Interferometry*. Academic Press, 1997.
- [4] A. Derevianko and S. G. Porsev. Determination of lifetimes of 6P(J) levels and ground-state polarizability of Cs from the van der Waals coefficient C-6. *Physical Review A*, 65(5), 2002.
- [5] A. Derevianko, W. R. Johnson, M. S. Safronova, and J. F. Babb. High-precision calculations of dispersion coefficients, static dipole polarizabilities, and atom-wall interaction constants for alkali-metal atoms. *Physical Review Letters*, 82(18):3589, 1999.
- [6] C.R. Hagen. Polarizabilities of atoms and molecules, new insights into an old subject. *Vacuum*, 58(2-3):117, 2000.
- [7] P. Kharchenko, J. F. Babb, and A. Dalgarno. Long-range interactions of sodium atoms. *Physical Review A*, 55(5):3566, 1997.
- [8] L. Kronik, I. Vasiliev, M. Jain, and J. R. Chelikowsky. Ab initio structures and polarizabilities of sodium clusters. *Journal of Chemical Physics*, 119(9):4322, 2001.
- [9] M. Seth J. K. Laerdahl P. Schwerdtfeger et al. I. S. Lim, M. Pernpointner. Relativistic coupled-cluster static dipole polarizabilities of the alkali metals from Li to element 119. *Physical Review A*, 60(4):2822, 1999.
- [10] G. Maroulis. On the static electric polarizability and hyperpolarizability of sodium. How good is the agreement between theory and experiment for the dipole polarizability? *Chemical Physics Letters*, 334(1-3):207, 2001.
- [11] M. Rerat, M. Merawa, and B. Honvault-Bussery. Ab initio calculations of dipole polarizabilities of Na and K in their 3(2)D-state and determination of long-range coefficients for S+D molecular states of Na-2, K-2, and NaK. *Journal of Chemical Physics*, 109(17):7246, 1998.

- [12] W. R. Johnson M. S. Safronova and A. Derevianko. Relativistic many-body calculations of energy levels, hyperfine constants, electric-dipole matrix elements, and static polarizabilities for alkali-metal atoms. *Physical Review A*, 60(6):4476, 1999.
- [13] A. J. Thakkar and C. Lupinetti. The polarizability of sodium: theory and experiment reconciled. *Chemical Physical Letters*, 402:270–273, 2005.
- [14] T.D. Roberts, A.D. Cronin, M.V. Tidberg, and D.E. Pritchard. Dispersion compensation for atom interferometry. *Phys. Rev. Lett*, 92(6):060405, 2004.
- [15] D. J. Griffiths. *Introduction to Electrodynamics*. Prentice Hall, Englewood Cliffs, New Jersey 07632, second edition, 1989.
- [16] D. C. Ghosh and R. Biswas. Theoretical Calculations of Absolute Radii of Atoms and Ions. Part 1. The Atomic Radii. *International Journal of Molecular Sciences*, 3:87–113, 2002.
- [17] J. D. Jackson. *Classical Electrodynamics*. John Wiley & Sons, third edition, 1999.
- [18] C. R. Ekstrom. *Experiments with a Separated Beam Atom Interferometer*. PhD thesis, Massachusetts Institute of Technology, 1993.
- [19] A. Dalgarno and A. E. Kingston. Van der Waals forces. *Proceedings of the Physical Society of London*, 73:455–464, 1959.
- [20] T. D. Roberts. *Measuring Atomic Properties with an Atom Interferometer*. PhD thesis, Massachusetts Institute of Technology, 2002.
- [21] J. A. Cross. *Electrostatics: Principles, Problems and Applications*. Adam Hilger, Techno House, Redcliffe Way, Bristol, BS1 6NX, England, 1987.
- [22] F. S. Acton. *Numerical Methods That Work*. Harper & Row, 49 East 33rd Street, New York, N.Y. 10016, 1970.
- [23] R. B. Roberts. Thermal expansion reference data: silicon 300-850K. *Journal of Physics D: Applied Physics*, 14:L163–L166, 1981.
- [24] Corning Incorporated. Pyrex Glass Code 7740. Corning, New York 14831, 1991.
- [25] G. Wallis and D. I. Pomerantz. Field assisted glass-metal sealing. *Journal of Applied Physics*, 40(10):3946–3949, September 1969.